

1

2

3

4

5

Simultaneous Measurement of Oscillation Parameters in Beam and Atmospheric Neutrino Data from Tokai-to-Kamioka and Super-Kamiokande Experiments

6

Daniel Robert Clement Barrow

7

8

Magdalen College,
Oxford University

9

Version 1.0

10

A Dissertation Submitted to Oxford University
11 for the Degree of Doctor of Philosophy

13 **Simultaneous Measurement of**
14 **Oscillation Parameters in Beam and**
15 **Atmospheric Neutrino Data from**
16 **Tokai-to-Kamioka and**
17 **Super-Kamiokande Experiments**

18 *Abstract*

19 Lorem ipsum dolor sit amet, consectetur adipiscing elit, sed do eiusmod tempor incididunt ut labore et dolore magna aliqua. Nulla aliquet porttitor lacus luctus accumsan tortor posuere. Pulvinar neque laoreet suspendisse interdum. Sem viverra aliquet eget sit. Nunc sed velit dignissim sodales ut eu sem integer vitae. At erat pellentesque adipiscing commodo elit at imperdiet dui accumsan. Fames ac turpis egestas integer eget aliquet nibh. Scelerisque eu ultrices vitae auctor eu augue. Purus non enim praesent elementum facilisis leo vel. Sollicitudin nibh sit amet commodo. Vitae auctor eu augue ut. Vel quam elementum pulvinar etiam. A condimentum vitae sapien pellentesque habitant morbi tristique senectus. Viverra accumsan in nisl nisi scelerisque eu ultrices. Sed viverra ipsum nunc aliquet bibendum enim. Sit amet purus gravida quis. In vitae turpis massa sed elementum tempus egestas sed sed. Vivamus arcu felis bibendum ut tristique et egestas. Senectus et netus et malesuada fames ac turpis. Ac auctor augue mauris augue.

35

Declaration

36

This dissertation is the result of my own work, except where explicit reference is made to the work of others, and has not been submitted for another qualification to this or any other university. This dissertation does not exceed the word limit for the respective Degree Committee.

37

38

39

40

41

Daniel Robert Clement Barrow

42

43

44

45

46

©The copyright of this thesis rests with the author and is made available under a Creative Commons Attribution Non-Commercial No Derivatives licence. Researchers are free to copy, distribute or transmit the thesis on the condition that they attribute it, that they do not use it for commercial purposes and that they do not alter, transform or build upon it. For any reuse or redistribution, researchers must make clear to others the licence terms of this work.

47

Acknowledgements

48 at pretium nibh ipsum. Eget nunc scelerisque viverra mauris in aliquam. Arcu vitae
49 elementum curabitur vitae nunc sed velit dignissim. Sed arcu non odio euismod lacinia
50 at quis risus sed. Vitae tempus quam pellentesque nec nam aliquam sem et tortor.
51 Viverra aliquet eget sit amet tellus cras adipiscing. Purus sit amet luctus venenatis
52 lectus magna. In aliquam sem fringilla ut morbi tincidunt augue. Fermentum dui
53 faucibus in ornare. Aliquam malesuada bibendum arcu vitae elementum curabitur
54 vitae nunc sed.

55 Ultricies leo integer malesuada nunc vel risus commodo. Tellus cras adipiscing
56 enim eu turpis egestas pretium. Dictumst quisque sagittis purus sit amet volutpat
57 consequat mauris nunc. Vitae congue mauris rhoncus aenean vel elit scelerisque
58 mauris pellentesque. Vel facilisis volutpat est velit egestas dui id ornare. Suscipit
59 adipiscing bibendum est ultricies. At in tellus integer feugiat scelerisque varius
60 morbi enim. Cras semper auctor neque vitae tempus. Commodo sed egestas egestas
61 fringilla phasellus faucibus. Cras pulvinar mattis nunc sed blandit. Pretium viverra
62 suspendisse potenti nullam ac tortor vitae. Purus sit amet volutpat consequat. Orci
63 sagittis eu volutpat odio facilisis mauris. Sit amet massa vitae tortor condimentum
64 lacinia quis. Commodo sed egestas egestas fringilla phasellus. Sed libero enim sed
65 faucibus turpis. Vitae tempus quam pellentesque nec.

66 Blandit massa enim nec dui. Viverra tellus in hac habitasse platea dictumst vestibulum.
67 Bibendum enim facilisis gravida neque convallis. Sagittis nisl rhoncus mattis
68 rhoncus urna neque. Nisl rhoncus mattis rhoncus urna neque. Ac tortor vitae purus
69 faucibus ornare. Aenean sed adipiscing diam donec adipiscing tristique risus. Sapien
70 nec sagittis aliquam malesuada bibendum. Et leo duis ut diam quam nulla. Tellus
71 rutrum tellus pellentesque eu tincidunt tortor aliquam nulla facilisi. Fermentum leo
72 vel orci porta non pulvinar neque. Eget sit amet tellus cras adipiscing enim eu. Sed
73 viverra tellus in hac habitasse platea dictumst vestibulum.

74 Sit amet consectetur adipiscing elit. At varius vel pharetra vel turpis nunc eget
75 lorem. Elit scelerisque mauris pellentesque pulvinar pellentesque habitant morbi
76 tristique senectus. Odio euismod lacinia at quis risus sed vulputate odio. Vitae suscipit
77 tellus mauris a diam maecenas sed enim ut. Dignissim convallis aenean et tortor at
78 risus viverra. Diam sollicitudin tempor id eu. Erat velit scelerisque in dictum. Blandit
79 cursus risus at ultrices. Ac tortor vitae purus faucibus ornare suspendisse sed.

⁸⁰ Contents

⁸¹ 1 Neutrino Oscillation Physics	¹
⁸² 1.1 Discovery of Neutrinos	¹
⁸³ 1.2 Theory of Neutrino Oscillation	²
⁸⁴ 1.2.1 Three Flavour Oscillations	³
⁸⁵ 1.2.2 The MSW Effect	⁶
⁸⁶ 1.3 Neutrino Oscillation Measurements	⁷
⁸⁷ 1.3.1 Solar Neutrinos	⁸
⁸⁸ 1.3.2 Atmospheric Neutrinos	¹⁰
⁸⁹ 1.3.3 Accelerator Neutrinos	¹²
⁹⁰ 1.3.4 Reactor Neutrinos	¹⁵
⁹¹ 2 T2K and SK Experiment Overview	¹⁷
⁹² 2.1 The Super-Kamiokande Experiment	¹⁷
⁹³ 2.1.1 The SK Detector	¹⁸
⁹⁴ 2.1.2 Calibration	²¹
⁹⁵ 2.1.3 Data Acquisition and Triggering	²³
⁹⁶ 2.1.4 Cherenkov Radiation	²⁵
⁹⁷ 2.2 The Tokai to Kamioka Experiment	²⁶
⁹⁸ 2.2.1 The Neutrino Beam	²⁸
⁹⁹ 2.2.2 The Near Detector at 280m	³¹
¹⁰⁰ 2.2.2.1 Fine Grained Detectors	³³
¹⁰¹ 2.2.2.2 Time Projection Chambers	³⁴
¹⁰² 2.2.2.3 π^0 Detector	³⁵
¹⁰³ 2.2.2.4 Electromagnetic Calorimeter	³⁶
¹⁰⁴ 2.2.2.5 Side Muon Range Detector	³⁸
¹⁰⁵ 2.2.3 The Interactive Neutrino GRID	³⁸
¹⁰⁶ 3 Bayesian Statistics Implemented Through Markov Chain Monte Carlo Techniques	⁴⁰
¹⁰⁸ 3.1 Bayesian Statistics	⁴¹
¹⁰⁹ 3.2 Monte Carlo Simulation	⁴²
¹¹⁰ 3.2.1 Markov Chain Monte Carlo	⁴³
¹¹¹ 3.2.2 Metropolis-Hastings Algorithm	⁴⁵

112	3.2.3 MCMC Optimisation	46
113	3.3 Understanding the MCMC Results	49
114	3.3.1 Marginalisation	50
115	3.3.2 Parameter Estimation and Credible Intervals	51
116	3.3.3 Application of Bayes' Theorem	52
117	3.3.4 Comparison of MCMC Output to Expectation	53
118	Bibliography	55
119	List of Figures	62
120	List of Tables	66

¹²² **Chapter 1**

¹²³ **Neutrino Oscillation Physics**

¹²⁴ When first proposed, neutrinos were expected to be massless fermions that only in-
¹²⁵ teract through weak and gravitational forces. This meant they were very difficult to
¹²⁶ detect as they can pass through significant amounts of matter without interacting. De-
¹²⁷ spite this, experimental neutrino physics has developed with many different detection
¹²⁸ techniques and neutrino sources being used today. In direct tension with the standard
¹²⁹ model physics, neutrinos have been determined to oscillate between different lepton
¹³⁰ flavours requiring them to have mass.

¹³¹ section 1.1 describes the observation techniques and discovery of neutrinos. The
¹³² theory underpinning neutrino oscillation is described in section 1.2. This section
¹³³ includes the approximations which can be made to simplify the understanding of
¹³⁴ neutrino oscillation in a two-flavour approximation as well as how the medium
¹³⁵ in which neutrinos propagate can manipulate the oscillation probability. The past,
¹³⁶ current, and future neutrino experiments are detailed in section 1.3 including the
¹³⁷ reactor, atmospheric, and long-baseline accelerator neutrino sources that have been
¹³⁸ used to successfully constrain oscillation parameter determination.

¹³⁹ **1.1 Discovery of Neutrinos**

¹⁴⁰ At the start of the 20th century, the electrons emitted from the β -decay of the nucleus
¹⁴¹ were found to have a continuous energy spectrum [1, 2]. This observation seemingly
¹⁴² broke the energy conservation invoked within that period’s nuclear models. Postulated
¹⁴³ in 1930 by Pauli as the solution to this problem, the neutrino (originally termed
¹⁴⁴ “neutron”) was theorized to be an electrically neutral spin-1/2 fermion with a mass of
¹⁴⁵ the same order of magnitude as the electron [3]. This neutrino was to be emitted with
¹⁴⁶ the electron in β -decay to alleviate the apparent breaking of energy conservation. As a
¹⁴⁷ predecessor of the weak interaction model, Fermi’s theory of β -decay developed the
¹⁴⁸ understanding by coupling the four constituent particles; electron, proton, neutron,
¹⁴⁹ and neutrino, into a consistent model [4].

Whilst Pauli was not convinced of the ability to detect neutrinos. The first observations of the particle were made in the mid-1950s when neutrinos from a reactor were observed via the inverse β -decay (IBD) process, $\bar{\nu}_e + p \rightarrow n + e^+$ [5, 6]. The detector consisted of two parts; a neutrino interaction medium and a liquid scintillator. The interaction medium was built from two water tanks. These were loaded with cadmium chloride to allow increased efficiency of neutron capture. The positron emitted from IBD annihilates, $e^+ + e^- \rightarrow 2\gamma$, generating a prompt signal and the neutron is captured on the cadmium via $n + {}^{108}Cd \rightarrow {}^{109}Cd \rightarrow {}^{109}Cd + \gamma$, producing a delayed signal. The experiment observed an increase in the neutrino event rate when the reactor was operating compared to when it was switched off, in much the same way as modern reactor neutrino experiments operate.

After the discovery of the ν_e , the natural question of how many flavours of neutrino exist was asked. In 1962, a measurement of the ν_μ was conducted at the Brookhaven National Laboratory [7]. A proton beam was directed at a beryllium target, generating a π -dominated beam which then decayed via $\pi^\pm \rightarrow \mu^\pm + (\nu_\mu, \bar{\nu}_\mu)$, and the subsequent interactions of the ν_μ were observed. The final observation to be made was that of the ν_τ from the DONUT experiment [8]. Three neutrinos seem the obvious solution as it mirrors the known number of charged lepton (as they form weak isospin doublets) but there could be evidence of more. Several neutrino experiments have found anomalous results [9, 10] which could be attributed to sterile neutrinos however cosmological observations indicate the number of neutrino species $N_{eff} = 3.15 \pm 0.23$ [11].

1.2 Theory of Neutrino Oscillation

As direct evidence of beyond Standard Model physics, a neutrino generated with lepton flavour α can change into a different lepton flavour β after propagating some distance. This phenomenon is called neutrino oscillation and requires that neutrinos must have a non-zero mass (as seen in subsection 1.2.1). This is direct evidence of beyond standard model physics. This behaviour has been characterised by the Pontecorvo-Maki-Nakagawa-Sakata (PMNS) [12–14] mixing matrix which describes how the flavour and mass of neutrinos are associated. This is analogous to the Cabibbo-Kobayashi-Maskawa (CKM) [15] matrix measured in quark physics.

¹⁸⁰ 1.2.1 Three Flavour Oscillations

¹⁸¹ The PMNS parameterisation defines three flavour eigenstates, ν_e , ν_μ and ν_τ (indexed
¹⁸² ν_α), which are assigned based upon the weak interaction flavour states and three mass
¹⁸³ eigenstates, ν_1 , ν_2 and ν_3 (indexed ν_i). Each mass eigenstate is the superposition of all
¹⁸⁴ three flavour states,

$$|\nu_i\rangle = \sum_{\alpha} U_{\alpha i} |\nu_{\alpha}\rangle. \quad (1.1)$$

¹⁸⁵ U is the PMNS matrix which correlates the mass and flavour eigenstates. Neutrinos
¹⁸⁶ interact with leptons of the same weak flavour eigenstate rather than mass eigenstate.
¹⁸⁷ The propagation of a neutrino flavour eigenstate, in a vacuum, can be re-written as a
¹⁸⁸ plane-wave solution to the time-dependent Schrödinger equation,

$$|\nu_{\alpha}(t)\rangle = \sum_i U_{\alpha i}^* |\nu_i\rangle e^{-i\phi_i}. \quad (1.2)$$

¹⁸⁹ The probability of observing a neutrino of flavour eigenstate β from one which
¹⁹⁰ originated as flavour α can be calculated as,

$$P(\nu_{\alpha} \rightarrow \nu_{\beta}) = |\langle \nu_{\beta} | \nu_{\alpha}(t) \rangle|^2 = \sum_{i,j} U_{\alpha i}^* U_{\beta i} U_{\alpha j} U_{\beta j}^* e^{-i(\phi_j - \phi_i)} \quad (1.3)$$

¹⁹¹ The ϕ_i term can be expressed in terms of the energy, E_i , and magnitude of the
¹⁹² three momenta, p_i , of the neutrino, $\phi_i = E_i t - p_i x$ (t and x being time and position
¹⁹³ coordinates). Therefore,

$$\phi_j - \phi_i = E_j t - E_i t - p_j x + p_i x. \quad (1.4)$$

¹⁹⁴ For a relativistic particle, $E_i \gg m_i$,

$$p_i = \sqrt{E_i^2 - m_i^2} \approx E_i - \frac{m_i^2}{2E_i}. \quad (1.5)$$

¹⁹⁵ Making the approximations that neutrinos are relativistic, the mass eigenstates
¹⁹⁶ were created with the same energy and that $x = L$, where L is the distance traveled by
¹⁹⁷ the neutrino, Equation 1.4 then becomes

$$\phi_j - \phi_i = \frac{\Delta m_{ij}^2 L}{2E}, \quad (1.6)$$

¹⁹⁸ where $\Delta m_{ij}^2 = m_i^2 - m_j^2$. This, teamed with further use of unitarity relations results
¹⁹⁹ in Equation 1.3 becoming

$$P(\nu_\alpha \rightarrow \nu_\beta) = \delta_{\alpha\beta} - 4 \sum_{i>j} \Re \left(U_{\alpha i}^* U_{\beta i} U_{\alpha j} U_{\beta j}^* \right) \sin^2 \left(\frac{\Delta m_{ij}^2 L}{4E} \right) + (-) 2 \sum_{i>j} \Im \left(U_{\alpha i}^* U_{\beta i} U_{\alpha j} U_{\beta j}^* \right) \sin \left(\frac{\Delta m_{ij}^2 L}{2E} \right). \quad (1.7)$$

²⁰⁰ Where $\delta_{\alpha\beta}$ is the Kronecker delta function and the negative sign is included for the
²⁰¹ oscillation probability of antineutrinos.

²⁰² Typically, the PMNS matrix is parameterised into three mixing angles, a charge
²⁰³ parity (CP) violating phase δ_{CP} , and two Majorana phases $\alpha_{1,2}$,

$$U = \underbrace{\begin{pmatrix} 1 & 0 & 0 \\ 0 & c_{23} & s_{23} \\ 0 & -s_{23} & c_{23} \end{pmatrix}}_{\text{Atmospheric, Accelerator}} \underbrace{\begin{pmatrix} c_{13} & 0 & s_{13}e^{-i\delta_{CP}} \\ 0 & 1 & 0 \\ -s_{13}e^{-i\delta_{CP}} & 0 & c_{13} \end{pmatrix}}_{\text{Reactor, Accelerator}} \underbrace{\begin{pmatrix} c_{12} & s_{12} & 0 \\ -s_{12} & c_{12} & 0 \\ 0 & 0 & 1 \end{pmatrix}}_{\text{Reactor, Solar}} \underbrace{\begin{pmatrix} e^{i\alpha_1/2} & 0 & 0 \\ 0 & e^{i\alpha_2/2} & 0 \\ 0 & 0 & 1 \end{pmatrix}}_{\text{Majorana}}. \quad (1.8)$$

204 Where $s_{ij} = \sin(\theta_{ij})$ and $c_{ij} = \cos(\theta_{ij})$. The oscillation parameters are often
205 grouped; (1,2) as “solar”, (2,3) as “atmospheric” and (1,3) as “reactor”. Many
206 neutrino experiments aim to measure the PMNS parameters from a wide array of
207 origins, as is the purpose of this thesis.

208 The Majorana phase, $\alpha_{1,2}$, containing matrix included within Equation 1.8 is only
209 included for completeness. For an oscillation analysis experiment, any term in this
210 oscillation probability calculation containing this phase disappears due to taking the
211 expectation value of the PMNS matrix.

212 A two flavour approximation can be attained when one assumes the third mass
213 eigenstate is degenerate with another. As discussed in section 1.3, it is found that
214 $\Delta m_{21}^2 \ll |\Delta m_{31}^2|$. This results in the two flavour approximation being reasonable for
215 understanding the features of the oscillation. In this two flavour case, the mixing
216 matrix becomes,

$$U_{2\text{ Flav.}} = \begin{pmatrix} \cos(\theta) & \sin(\theta) \\ -\sin(\theta) & \cos(\theta) \end{pmatrix}. \quad (1.9)$$

217 This culminates in the oscillation probability,

$$\begin{aligned} P(\nu_\alpha \rightarrow \nu_\alpha) &= 1 - \sin^2(2\theta) \sin^2\left(\frac{\Delta m^2 L}{4E}\right), \\ P(\nu_\alpha \rightarrow \nu_\beta) &= \sin^2(2\theta) \sin^2\left(\frac{\Delta m^2 L}{4E}\right). \end{aligned} \quad (1.10)$$

218 For $\alpha \neq \beta$. For a fixed neutrino energy, the oscillation probability is a sinusoidal
219 function depending upon the distance over which the neutrino propagates. The
220 frequency and amplitude of oscillation are dependent upon the ratio of the $\Delta m^2/4E$
221 and $\sin^2 2\theta$, respectively. For more human-readable units, the maximum oscillation
222 probability for a fixed value of θ is given at $L[\text{km}]/E[\text{GeV}] \sim 1.27/\Delta m^2$. It is this
223 calculation that determines the best L/E value for a given experiment to be designed
224 around for measurements of a specific value of Δm^2 .

²²⁵ 1.2.2 The MSW Effect

²²⁶ The theory of neutrino oscillation in a vacuum is described in subsection 1.2.1. How-
²²⁷ ever, the beam neutrinos and atmospheric neutrinos originating from below the
²²⁸ horizon propagate through matter in the Earth. The coherent scattering of neutrinos
²²⁹ from a material target modifies the hamiltonian of the system. This results in a change
²³⁰ in the oscillation probability. Notably, charged current scattering ($\nu_e + e^- \rightarrow \nu_e + e^-$,
²³¹ propagated by a W boson) only affects electron neutrinos compared to the neutral
²³² current scattering ($\nu_l + l^- \rightarrow \nu_l + l^-$, propagated by a Z^0 boson), interacts through
²³³ all neutrino flavours equally. In the two-flavour limit, the effective mixing parameter
²³⁴ becomes

$$\sin^2(2\theta) \rightarrow \sin^2(2\theta_m) = \frac{\sin^2(2\theta)}{(A/\Delta m^2 - \cos(2\theta))^2 + \sin^2(2\theta)}, \quad (1.11)$$

²³⁵ where $A = 2\sqrt{2}G_F N_e E$ with N_e is the electron density of the medium and G_F is
²³⁶ Fermi's constant. It is clear to see that there exists a value of $A = \Delta m^2 \cos(2\theta)$ for
²³⁷ $\Delta m^2 > 0$ which results in a divergent mixing parameter. This resonance is due to
²³⁸ the Mikheyev-Smirnov-Wolfenstein (MSW) effect (or more colloquially, the matter
²³⁹ resonance) which regenerates the electron neutrino component of the neutrino flux
²⁴⁰ [16–18]. The density at which the resonance occurs is given by

$$N_e = \frac{\Delta m^2 \cos(2\theta)}{2\sqrt{2}G_F E}. \quad (1.12)$$

²⁴¹ At densities lower than this critical value, the oscillation probability will be much
²⁴² closer to that of vacuum oscillation. The resonance occurring from the MSW effect
²⁴³ depends on the sign of Δm^2 . Therefore, any neutrino oscillation experiment which
²⁴⁴ observes neutrinos and antineutrinos which have propagated through matter can have
²⁴⁵ some sensitivity to the ordering of the neutrino mass eigenstates.

²⁴⁶ For an experiment observing atmospheric neutrinos propagating through the Earth,
²⁴⁷ such as the studies presented in this thesis, a model of the Earth's density and layering
²⁴⁸ is required. The model used within this analysis is the Preliminary Reference Earth

249 Model (PREM) [19]. This model provides piecewise cubic polynomials. To follow the
250 methodology set in [20], this analysis simply approximates the model as four layers of
251 constant density with values taken from the PREM model, as described in Table 1.1.
252 As seen in DB: [Link to Oscillation chapter](#), the approximation in this methodology has
253 been removed and the density is instead integrated along the track using the piecewise
254 polynomials.

255 The density measurements provided in the PREM model are provided in terms
256 of mass density, whereas neutrino oscillations are sensitive to the electron number
257 density. This value can be computed as the product of the chemical composition and
258 mass density of each layer.

Layer	Outer Radius [km]	Density [g/cm ³]	Chemical composition (Z/A)
Inner Core	1220	13	0.468 ± 0.029
Outer Core	3480	11.3	0.468 ± 0.029
Lower Mantle	5701	5.0	0.497
Transition Zone	6371	3.3	0.497

Table 1.1: Description of the four layers of the Earth invoked within the PREM model [19].

259 The beam oscillation probability in this thesis uses a baseline of 295km, density
260 2.6g/cm³, and chemical composition 0.5.

261 1.3 Neutrino Oscillation Measurements

262 As evidence of beyond standard model physics, the 2015 Nobel Prize in Physics was
263 awarded to the Super-Kamiokande (SK) [21] and Sudbury Neutrino Observatory
264 (SNO) [22] collaborations for the first definitive observation of solar and atmospheric
265 neutrino oscillation [23]. Since then, the field has seen a wide array of oscillation
266 measurements from a variety of neutrino sources. As seen in subsection 1.2.1, the
267 neutrino oscillation probability is dependent on the ratio of the propagation baseline, L ,
268 to the neutrino energy, E . It is this ratio that determines the type of neutrino oscillation
269 a particular experiment is sensitive to.

270 As illustrated in Figure 1.1, there are many neutrino sources that span a wide
271 range of energies. The least energetic neutrinos are from diffuse supernovae and

²⁷² terrestrial neutrinos at $O(1)$ MeV whereas the most energetic neutrinos originate from
²⁷³ atmospheric and galactic neutrinos of $> O(1)$ TeV.

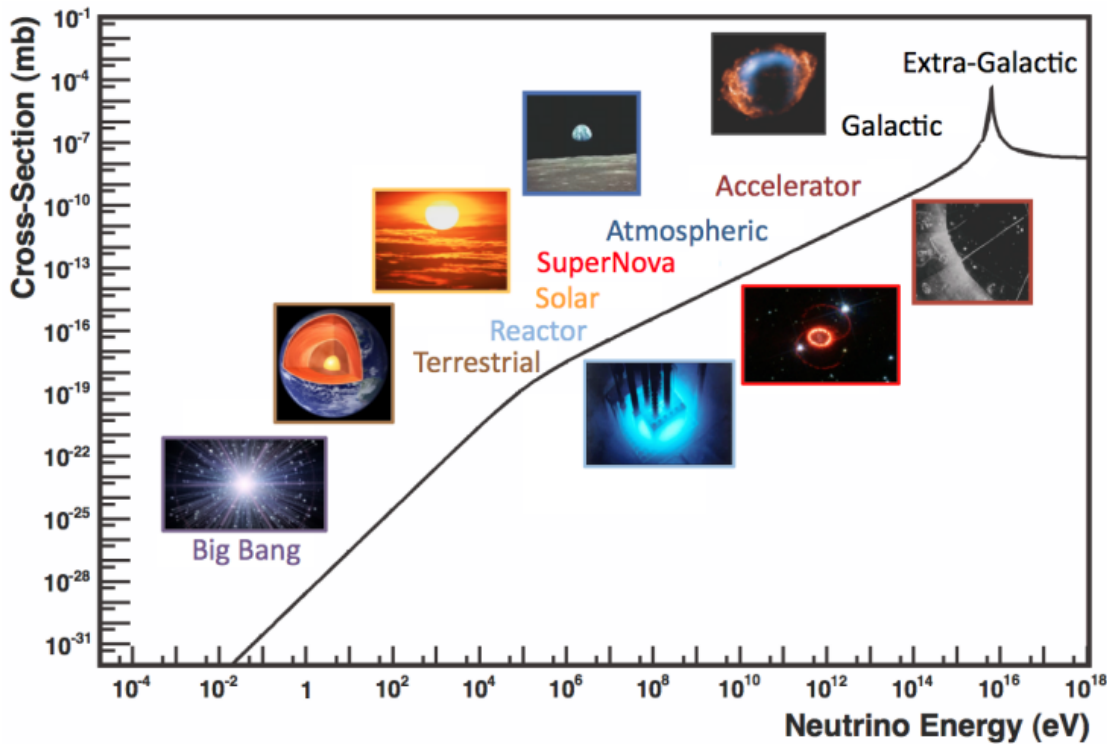


Figure 1.1: The cross-section of neutrinos from various natural and man-made sources as a function of neutrino energy. Taken from [24]

²⁷⁴ 1.3.1 Solar Neutrinos

²⁷⁵ Solar neutrinos are emitted from fusion reaction chains at the center of the Sun. The
²⁷⁶ solar neutrino flux, given as a function of neutrino energy for different fusion and
²⁷⁷ decay chains is illustrated in Figure 1.2. Whilst proton-proton fusion generates the
²⁷⁸ largest flux of neutrinos, the neutrinos are of low energy and are difficult to reconstruct
²⁷⁹ due to the IBD interaction threshold of 1.8MeV. Consequently, most experiments focus
²⁸⁰ on the neutrinos from the decay of 8B (via ${}^8B \rightarrow {}^8Be^* + e^+ + \nu_e$), which are higher
²⁸¹ energy.

²⁸² The first measurements of solar neutrinos observed a significant reduction in the
²⁸³ event rate compared to predictions from the Standard Solar Model [26, 27]. The
²⁸⁴ proposed solution to this “solar neutrino problem” was $\nu_e \leftrightarrow \nu_\mu$ oscillations in a

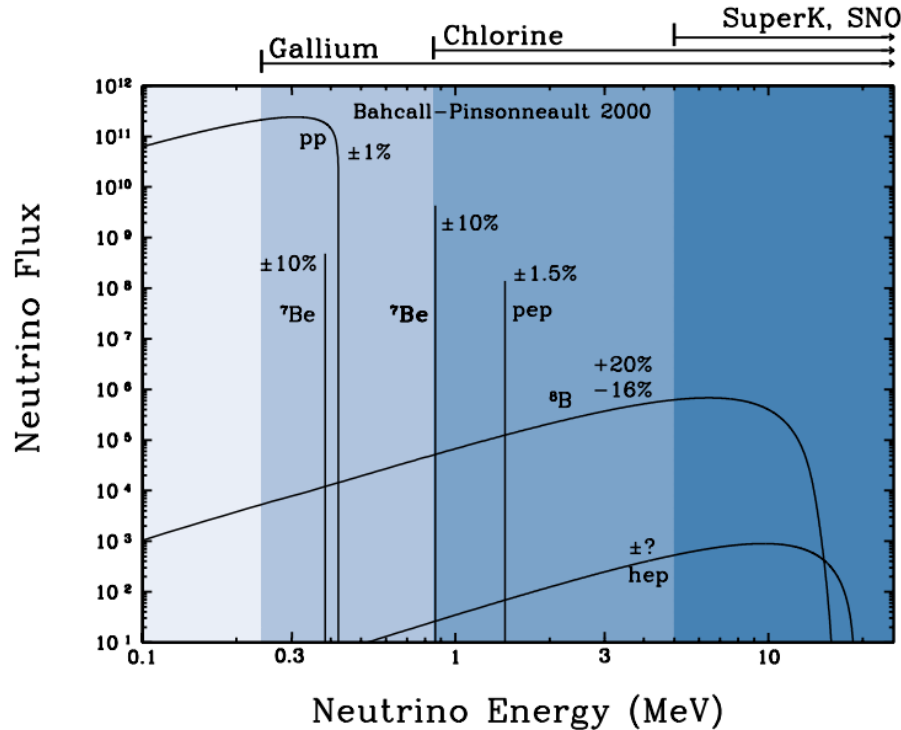


Figure 1.2: The solar neutrino flux as a function of neutrino energy for various fusion reactions and decay chains as predicted by the Standard Solar Model. Taken from [25].

285 precursory version of the PMNS model [28]. The Kamiokande [29], Gallex [30] and
286 Sage [31] experiments confirmed the ~ 0.5 factor deficit of solar neutrinos.

287 The conclusive solution to this problem was determined by the SNO collaboration
288 [32]. Using a deuterium water target to observe 8B neutrinos, the event rate of
289 charged current (CC), neutral current (NC), and elastic scattering (ES) interactions
290 (Given in Equation 1.13) was simultaneously measured. CC events can only occur for
291 electron neutrinos, whereas the other interaction channels are agnostic to neutrino
292 flavour (Although the ES reaction is more sensitive to electron neutrino interactions).
293 This meant that there were direct measurements of the ν_e and ν_x neutrino flux. It
294 was concluded that the CC and ES interaction rates were consistent with the deficit
295 previously observed. Most importantly, the NC reaction rate was only consistent with
296 the others under the hypothesis of flavour transformation.

$$\begin{aligned}
 \nu_e + d &\rightarrow p + p + e^- & (CC) \\
 \nu_x + d &\rightarrow p + n + \nu_x & (NC) \\
 \nu_x + e^- &\rightarrow \nu_x + e^- & (ES)
 \end{aligned} \tag{1.13}$$

Many experiments have since measured the neutrino flux of different interaction chains within the sun [33–35]. The most recent measurement was that of CNO neutrinos which were recently observed with 5σ significance by the Borexino collaboration. Future neutrino experiments aim to further these spectroscopic measurements of different fusion chains within the Sun [36–38]. Solar neutrinos act as an irreducible background for dark matter experiments like DARWIN but oscillation parameter measurements can be made [39].

1.3.2 Atmospheric Neutrinos

The interactions of primary cosmic ray protons in Earth's upper atmosphere generate showers of energetic hadrons. These are mostly pions and kaons which when they decay produce a natural source of neutrinos spanning energies of MeV to TeV [40]. This decay is via

$$\begin{aligned}
 \pi^\pm &\rightarrow \mu^\pm + (\nu_\mu, \bar{\nu}_\mu) \\
 \mu^\pm &\rightarrow e^\pm + (\nu_\mu, \bar{\nu}_\mu) + (\nu_e, \bar{\nu}_e)
 \end{aligned} \tag{1.14}$$

such that for a single pion decay, three neutrinos are produced. The atmospheric neutrino flux energy spectra as predicted by the Bartol [41], Honda [42, 43], and FLUKA [44] models are illustrated in Figure 1.3. The flux distribution peaks at an energy of $O(10)$ GeV. The uncertainties associated with these models are dominated by the hadronic production of kaon and pions as well as the primary cosmic flux.

Unlike long-baseline experiments which have a fixed baseline, the distance atmospheric neutrinos propagate is dependent upon the zenith angle at which they interact. This is illustrated in Figure 1.4. Neutrinos that are generated directly above the detector ($\cos(\theta) = 1.0$) have a baseline equivalent to the height of the atmosphere whereas neutrinos that interact directly below the detector ($\cos(\theta) = -1.0$) have to

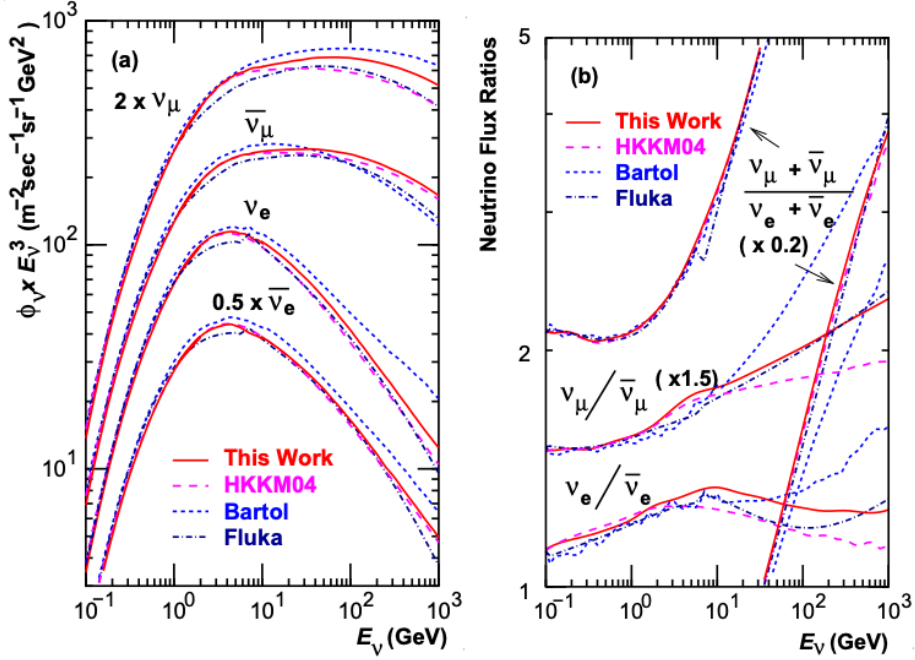


Figure 1.3: Left panel: The atmospheric neutrino flux for different neutrino flavours as a function of neutrino energy as predicted by the 2007 Honda model (“This work”) [42], the 2004 Honda model (“HKKM04”) [43], the Bartol model [41] and the FLUKA model [44]. Right panel: The ratio of the muon to electron neutrino flux as predicted by all the quoted models. Both figures taken from [42].

319 travel a length equal to the diameter of the Earth. This means atmospheric neutrinos
 320 have a baseline that varies from $O(20)$ km to $O(6 \times 10^3)$ km. Any neutrino generated
 321 at or below the horizon will be subject to matter effects as they propagate through the
 322 Earth.

323 Figure 1.5 highlights the neutrino flux as a function of the zenith angle for different
 324 slices of neutrino energy. For medium to high-energy neutrinos (and to a lesser degree
 325 for low-energy neutrinos), the flux is approximately symmetric around $\cos(\theta) = 0$.
 326 To the accuracy of this approximation, the systematic uncertainties associated with
 327 atmospheric flux for comparing upward-going and down-going neutrino cancels. This
 328 allows the down-going events, which are mostly insensitive to oscillation probabilities,
 329 to act as an unoscillated prediction (similar to a near detector in an accelerator neutrino
 330 experiment).

331 Precursory hints of atmospheric neutrinos were observed in the mid-1960s search-
 332 ing for $\nu_\mu^{(-)} + X \rightarrow X^* + \mu^\pm$ [46]. This was succeeded with the IMB-3 [47] and
 333 Kamiokande [48] experiments which measured the ratio of muon neutrinos com-
 334 pared to electron neutrinos $R(\nu_\mu/\nu_e)$. Both experiments were found to have a con-

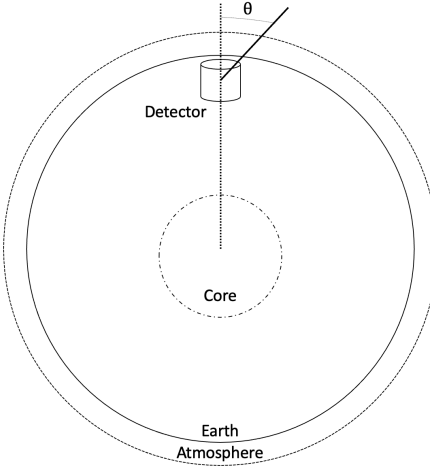


Figure 1.4: A diagram illustrating the definition of zenith angle as used in the Super Kamiokande experiment [45].

³³⁵ sistent deficit of muon neutrinos, with $R(\nu_\mu/\nu_e) = 0.67 \pm 0.17$ and $R(\bar{\nu}_\mu/\bar{\nu}_e) =$
³³⁶ $0.60^{+0.07}_{-0.06} \pm 0.05$. Super-Kamiokande (SK) [45] extended this analysis by fitting os-
³³⁷ cillation parameters in $P(\nu_\mu \rightarrow \nu_\tau)$ which found best fit parameters $\sin^2(2\theta) > 0.92$
³³⁸ and $1.5 \times 10^{-3} < \Delta m^2 < 3.4 \times 10^{-3} \text{ eV}^2$.

³³⁹ Since then, atmospheric neutrino experiments have been making precision mea-
³⁴⁰ surements of the $\sin^2(\theta_{23})$ and Δm^2_{32} oscillation parameters. Atmospheric neutrino
³⁴¹ oscillation is dominated by $P(\nu_\mu \rightarrow \nu_\tau)$, where SK observed a 4.6σ discovery of ν_τ
³⁴² appearance [49]. Figure 1.6 illustrates the current estimates on the atmospheric mixing
³⁴³ parameters from a wide range of atmospheric and accelerator neutrino observatories.

³⁴⁴ 1.3.3 Accelerator Neutrinos

³⁴⁵ The concept of using a man-made “neutrino beam” was first realised in 1962 [56].
³⁴⁶ Since then, many experiments have followed which all use the same fundamental
³⁴⁷ concepts. Typically, a proton beam is aimed at a target producing charged mesons that
³⁴⁸ decay to neutrinos. The mesons can be sign-selected by the use of magnetic focusing
³⁴⁹ horns to generate a neutrino or antineutrino beam. Pions are the primary meson that
³⁵⁰ decay and depending on the orientation of the magnetic field, a muon (anti-)neutrino
³⁵¹ beam is generated via $\pi^+ \rightarrow \mu^+ + \nu_\mu$ or $\pi^- \rightarrow \mu^- + \bar{\nu}_\mu$. The decay of muons and
³⁵² kaons does result in an irreducible intrinsic electron neutrino background. In T2K,
³⁵³ this background contamination is $O(< 1\%)$ [57]. There is also an approximately $\sim 5\%$
³⁵⁴ “wrong-sign” neutrino background of $\bar{\nu}_\mu$ generated via the same decays.

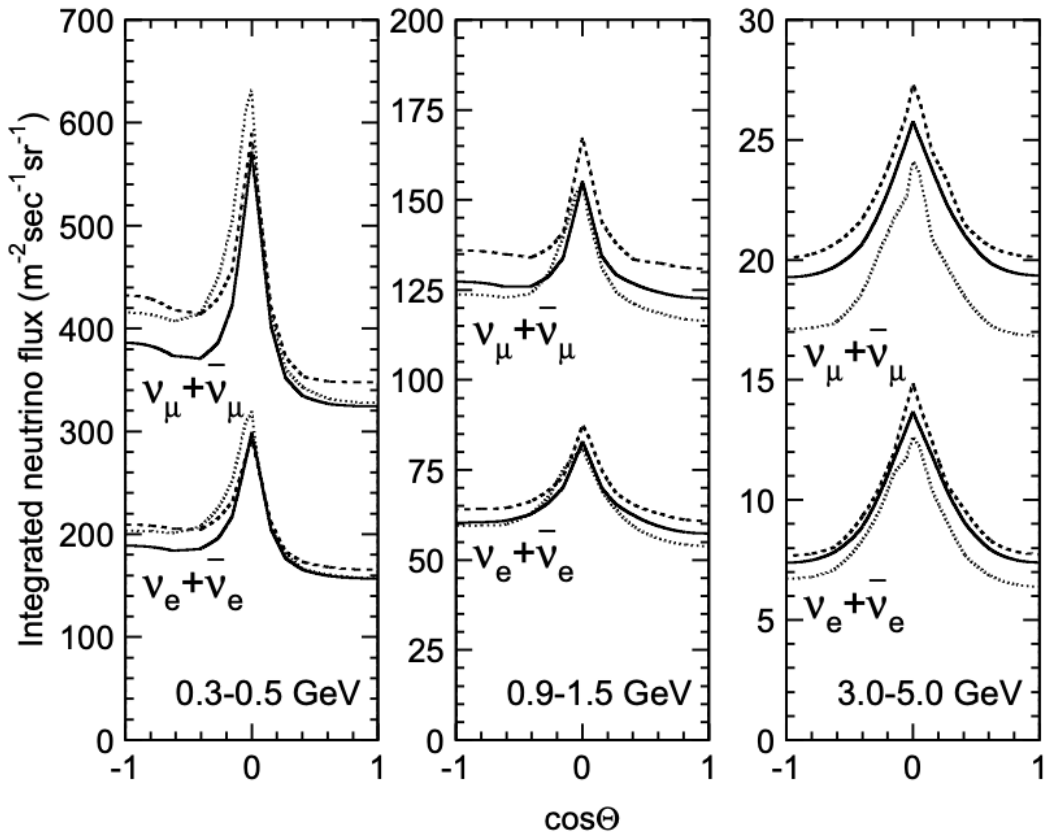


Figure 1.5: Predictions of the summed neutrino and antineutrino flux for electron and muon neutrinos from the Bartol [41], Honda [42] and FLUKA [44] models as a function of zenith angle with respect to the detector. Left panel: $0.3 < E_\nu < 0.5$. Middle panel: $0.9 < E_\nu < 1.5$. Right panel: $3.0 < E_\nu < 5.0$. Figures taken from [45].

The energy of each neutrino in the beam is dependent on the energy of the initial proton beam. Therefore, tuning the proton energy allows the neutrino energy to be set to a value that maximises the disappearance oscillation probability in the L/E term in Equation 1.10. This means that accelerator experiments are typically more sensitive to the mixing parameters as compared to a natural neutrino source. However, the disadvantage compared to atmospheric neutrino experiments is that the baseline has to be shorter due to the lower flux. Consequently, there is typically less sensitivity to matter effects and the ordering of the neutrino mass eigenstates.

A neutrino experiment measures

$$R(\vec{x}) = \Phi(E_\nu) \times \sigma(E_\nu) \times \epsilon(\vec{x}) \times P(\nu_\alpha \rightarrow \nu_\beta), \quad (1.15)$$

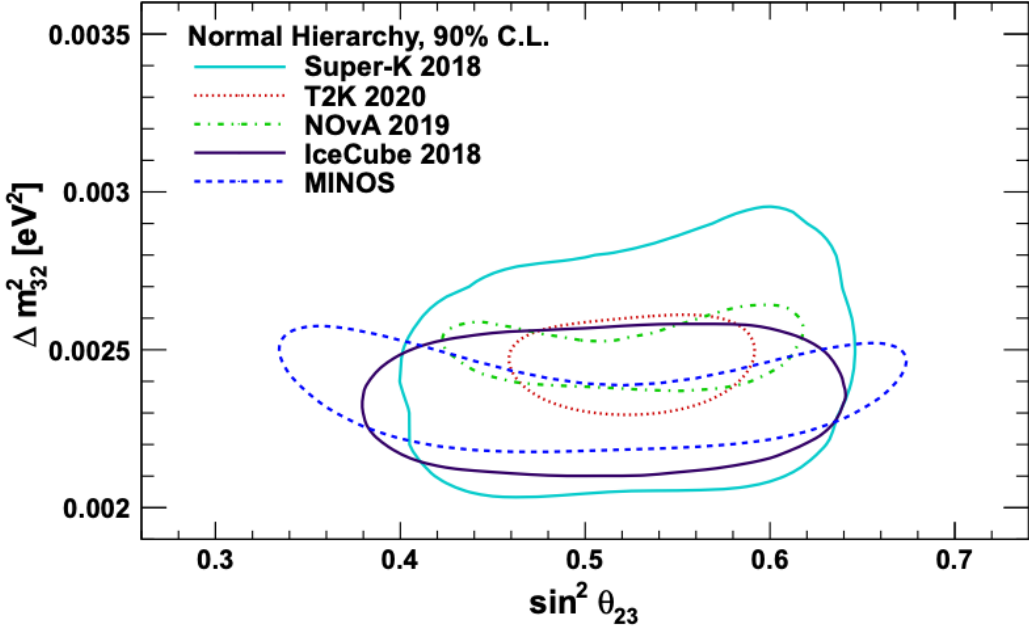


Figure 1.6: Constraints on the atmospheric oscillation parameters, $\sin^2(\theta_{23})$ and Δm_{23}^2 , from atmospheric and long baseline experiments: SK [50], T2K [51], NO ν A [52], IceCube [53] and MINOS [54]. Figure taken from [55].

where $R(\vec{x})$ is the event rate of neutrinos at position \vec{x} , $\Phi(E_\nu)$ is the flux of neutrinos with energy E_ν , $\sigma(E_\nu)$ is the cross-section of the neutrino interaction and $\epsilon(\vec{x})$ is the efficiency of the detector. In order to leverage the most out of an accelerator neutrino experiment, the flux and cross-section systematics need to be constrained. This is typically done via the use of a “near detector”, situated at a baseline of $O(1)$ km. This detector observes the unoscillated neutrino flux and constrains the parameters used within the flux and cross-section model.

The first accelerator experiments to precisely measure oscillation parameters were MINOS [58] and K2K [59]. These experiments confirmed the $\nu_\mu \rightarrow \nu_\mu$ oscillations seen in atmospheric neutrino experiments by finding consistent mixing parameter values for $\sin^2(\theta_{23})$ and Δm_{23}^2 . The current generation of accelerator neutrino experiments, T2K and NO ν A extended this field by observing $\bar{\nu}_\mu \rightarrow \bar{\nu}_e$ and lead the sensitivity to atmospheric mixing parameters as seen in Figure 1.6 [60]. The two experiments differ in their peak neutrino energy, baseline, and detection technique. The NO ν A experiment is situated at a baseline of 810km from the NuMI beamline which delivers 2GeV neutrinos. The T2K neutrino beam is peaked around 0.6GeV and propagates 295km. The NO ν A experiment also uses functionally identical detectors (near and far) which allow the approximate cancellation of detector systematics whereas T2K uses a plastic scin-

382 tillator technique at the near detector and a water Cherenkov far detector. The future
383 generation experiments DUNE [61] and Hyper-Kamiokande [62] will succeed these
384 experiments as the high-precision era of neutrino oscillation parameter measurements
385 develops.

386 Several anomalous results have been observed in the LSND [9] and MiniBooNE [10]
387 detectors which were designed with purposefully short baselines. Parts of the neu-
388 trino community attributed these results to oscillations induced by a fourth “sterile”
389 neutrino [63] but several searches in other experiments, MicroBooNE [64] and KAR-
390 MEN [65], found no hints of additional neutrino species. The solution to the anomalous
391 results are still being determined.

392 1.3.4 Reactor Neutrinos

393 As illustrated in the first discovery of neutrinos (section 1.1), nuclear reactors are a very
394 useful man-made source of electron antineutrinos. For reactors that use low-enriched
395 uranium ^{235}U as fuel, the antineutrino flux is dominated by the β -decay fission of ^{235}U ,
396 ^{238}U , ^{239}Pu and ^{241}Pu [66] as illustrated in Figure 1.7.

397 Due to their low energy, reactor electron antineutrinos predominantly interact
398 via the inverse β -decay (IBD) interaction. The typical signature contains two signals
399 delayed by $O(200)\mu\text{s}$; firstly the prompt photons from positron annihilation, and
400 secondly the photons emitted ($E_{tot}^\gamma = 2.2\text{MeV}$) from de-excitation after neutron capture
401 on hydrogen. Searching for both signals improves the detector’s ability to distinguish
402 between background and signal events [68]. Recently, SK included gadolinium dopants
403 into the ultra-pure water to increase the energy released from the photon cascade to
404 $\sim 8\text{MeV}$ and reduce the time of the delayed signal to $\sim 28\mu\text{s}$.

405 There are many short baseline experiments ($L \sim O(1)\text{km}$) that have measured
406 the $\sin^2(\theta_{13})$ and Δm_{23}^2 oscillation parameters. Daya Bay [69], RENO [70] and Double
407 Chooz [71] have all provided precise measurements, with the first discovery of a
408 non-zero θ_{13} made by Daya Bay and RENO (and complimented by T2K [71]). The
409 constraints on $\sin^2(\theta_{13})$ by the reactor experiments lead the field and are often used
410 as external inputs to accelerator neutrino experiments to improve their sensitivity to
411 δ_{CP} and mass hierarchy determination. JUNO-TAO [72], a small collaboration within
412 the larger JUNO experiment, is a next-generation reactor experiment that aims to
413 precisely measure the isotopic antineutrino yields from the different fission chains.

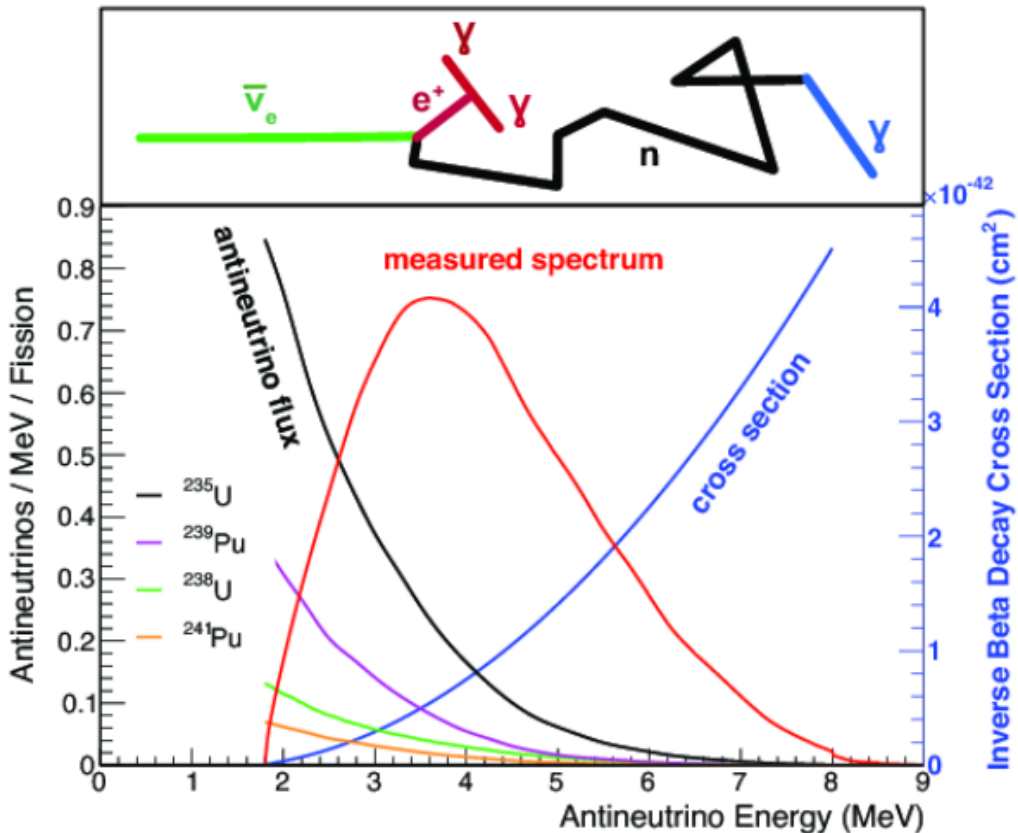


Figure 1.7: Reactor electron antineutrino fluxes for ^{235}U (Black), ^{238}U (Green), ^{239}Pu (Purple), and ^{241}Pu (Orange) isotopes. The inverse β -decay cross-section (Blue) and corresponding measurable neutrino spectrum (Red) are also given. Top panel: Schematic of Inverse β -decay interaction including the eventual capture of the emitted neutron. This capture emits a γ -ray which provides a second signal of the event. Taken from [67].

⁴¹⁴ Alongside this, it aims to explain the ‘5MeV excess’ [73–75] by conducting a search for
⁴¹⁵ sterile neutrinos with a mass scale of around 1eV.

⁴¹⁶ Kamland [76] is the only experiment to have observed reactor neutrinos using a
⁴¹⁷ long baseline (flux weighted averaged baseline of $L \sim 180\text{km}$) which allows it to have
⁴¹⁸ sensitivity to Δm_{12}^2 . Combined with the SK solar neutrino experiment, the combined
⁴¹⁹ analysis puts the most stringent constraint on Δm_{12}^2 [77] which is used as a prior
⁴²⁰ uncertainty within accelerator neutrino experiments.

⁴²¹ Chapter 2

⁴²² T2K and SK Experiment Overview

⁴²³ As the successor of the Kamiokande experiment, the Super-Kamiokande (SK) collaboration
⁴²⁴ has been leading atmospheric neutrino oscillation analyses for over two decades.
⁴²⁵ The detector has provided some of the strongest constraints on proton decay limits and
⁴²⁶ as well as the first precise measurements of the Δm_{23}^2 and $\sin^2(\theta_{23})$ neutrino oscillation
⁴²⁷ parameters. Despite this, the ability of the detector to low-energy neutrino events
⁴²⁸ has been significantly improved with the recent gadolinium doping of the ultra-pure
⁴²⁹ water target. section 2.1 describes the history, detection technique, and operation of
⁴³⁰ the SK detector.

⁴³¹ The Tokai-to-Kamioka (T2K) experiment was one of the first long-baseline experiments
⁴³² to use both neutrino and antineutrino beams to precisely measure the
⁴³³ charge parity violation within the neutrino sector. With the SK detector observing
⁴³⁴ the oscillated neutrino flux, the T2K experiment observed the first hints of a non-zero
⁴³⁵ $\sin^2(\theta_{13})$ measurement and continues to lead the field with the constraints it provides
⁴³⁶ on $\sin^2(\theta_{13})$, $\sin^2(\theta_{23})$, Δm_{23}^2 and δ_{CP} . section 2.2 documents the techniques which T2K
⁴³⁷ uses in generating its neutrino beam as well as the ‘near-detector’ used to constrain
⁴³⁸ the flux and cross-section parameters invoked within the systematic models.

⁴³⁹ 2.1 The Super-Kamiokande Experiment

⁴⁴⁰ The SK experiment began taking data in 1996 [78] and has had many modifications
⁴⁴¹ throughout its lifespan. There have been seven defined periods of data taking as
⁴⁴² noted in Table 2.1. Data taking began in SK-I which ran for five years. Between the
⁴⁴³ SK-I and SK-II periods, a significant proportion of the PMTs were damaged during
⁴⁴⁴ maintenance. Those that survived were equally distributed throughout the detector
⁴⁴⁵ in the SK-II era, which resulted in a reduced photo-coverage. From SK-III onwards,
⁴⁴⁶ repairs to the detector meant the full suite of PMTs was operational. Before the
⁴⁴⁷ start of SK-IV, the data acquisition and electronic systems were upgraded. Between
⁴⁴⁸ SK-IV and SK-V, a significant effort was placed into tank open maintenance and

449 repair/replacement of defective PMTs, a task for which the author of this thesis was
 450 required. Consequently, the detector conditions were significantly different between
 451 the two operational periods. SK-VI saw the start of the 0.01% gadolinium doped
 452 water. SK-VII, which started during the writing of this thesis, has increased the
 453 gadolinium concentration to 0.03% for continued operation. [DB: Link to Linyan's talk from Nu2022.](#)
 454

Period	Start Date	End Date	Live-time (days)
I	April 1996	July 2001	1489.19
II	October 2002	October 2005	798.59
III	July 2006	September 2008	518.08
IV	September 2008	May 2018	3244.4
V	January 2019	July 2020	461.02
VI	July 2020	May 2022	583.3
VII	May 2022	Ongoing	N/A

Table 2.1: The various SK periods and respective live-time. The SK-VI live-time is calculated until 1st April 2022. SK-VII started during the writing of this thesis.

455 2.1.1 The SK Detector

456 The basic structure of the Super-Kamiokande (SK) detector is a cylindrical tank with a
 457 diameter 39.3m and height 41.1m filled with ultrapure water [79]. A diagram of the
 458 significant components of the SK detector is illustrated in Figure 2.1. The SK detector
 459 is situated in the Kamioka mine in Gifu, Japan. The mine is underground with roughly
 460 1km rock overburden (2.7km water equivalent overburden) [80]. At this depth, the
 461 rate of cosmic ray muons is significantly decreased to a value of $\sim 2\text{Hz}$. The top of
 462 the tank is covered with stainless steel which is designed as a working platform for
 463 maintenance, calibration, and location for high voltage and data acquisition electronics.

464 A smaller cylindrical structure (36.2m diameter, 33.8m height) is situated inside the
 465 tank, with an approximate 2m gap between this structure and the outer tank wall. The
 466 purpose of this structure is to support the photomultiplier tubes (PMTs). The volume
 467 inside and outside the support structure is referred to as the inner detector (ID) and
 468 outer detector (OD), respectively. In the SK-IV era, the ID and OD are instrumented
 469 by 11,129 50cm and 1,885 20cm PMTs respectively [79]. The ID contains a 32kton
 470 mass of water. Many analyses performed at SK use a “fiducial volume” defined by the

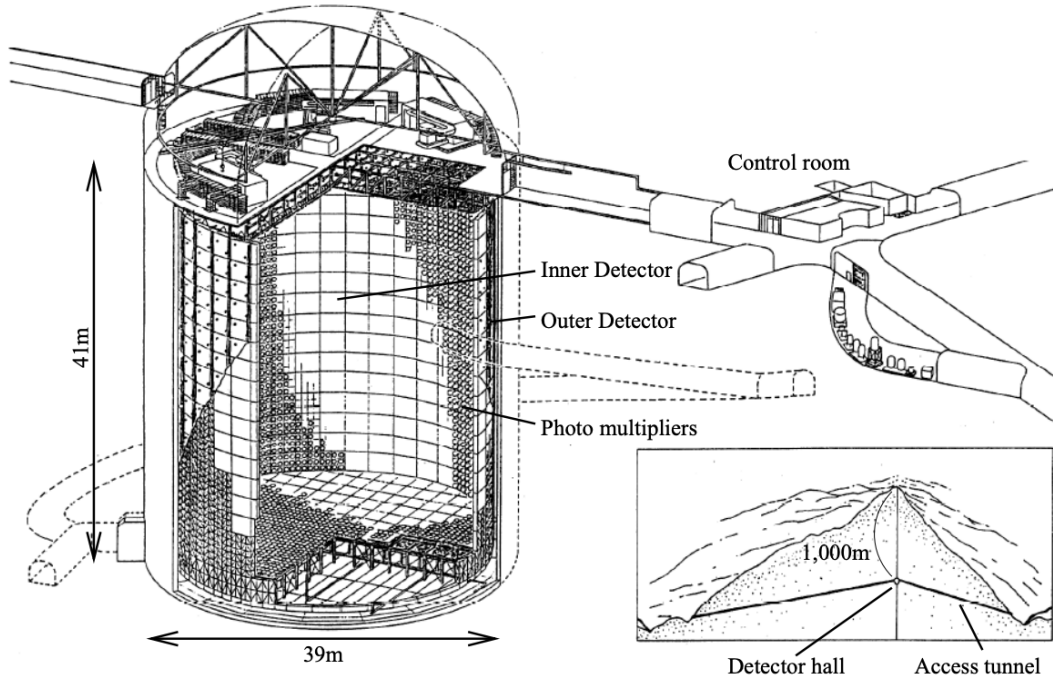


Figure 2.1: A schematic diagram of the Super-Kamiokande Detector. Taken from [81].

471 volume of water inside the ID excluding some distance to the ID wall. This reduces the
 472 volume of the detector which is sensitive to neutrino events but reduces radioactive
 473 backgrounds and allows for better reconstruction performance. The nominal fiducial
 474 volume is defined as the area contained inside 2m from the ID wall for a total of
 475 22.5kton water [82].

476 The two regions of the detector (ID and OD) are optically separated with opaque
 477 black plastic. The purpose of this is to determine whether a track entered or exited
 478 the ID. This allows cosmic ray muons and partially contained events to be tagged and
 479 separated from neutrino events entirely contained within the ID. This black plastic is
 480 also used to cover the area between the ID PMTs to reduce photon reflection from the
 481 ID walls. Opposite to this, the OD is lined with a reflective material to allow photons to
 482 reflect around inside the OD until collected by one of the PMTs. Furthermore, each OD
 483 PMT is backed with $50 \times 50\text{cm}$ plates of wavelength shifting acrylic which increases
 484 the efficiency of light collection [80].

485 In the SK-IV data-taking period, the photocathode coverage of the detector, or the
 486 fraction of the ID wall instrumented with PMTs, is $\sim 40\%$ [80]. The PMTs have a
 487 quantum efficiency (the ratio of detected electrons to incident photons) of $\sim 21\%$ for
 488 photons with wavelengths of $360\text{nm} < \lambda < 390\text{nm}$. The proportion of photoelectrons

489 that produce a signal in the dynode of a PMT, termed the collection efficiency, is
490 $> 70\%$ [80]. The PMTs used within SK are most sensitive to photons with wavelength
491 $300\text{nm} \leq \lambda \leq 600\text{nm}$ [80]. One disadvantage of using PMTs as the detection media
492 is that the Earth's geomagnetic field can modify its response. Therefore, a set of
493 compensation coils is built around the inner surface of the detector to mitigate this
494 effect [83].

495 As mentioned, the SK detector is filled with ultrapure water, which in a perfect
496 world would contain no impurities. However, bacteria and organic compounds can
497 significantly degrade the water quality. This decreases the attenuation length which
498 reduces the total number of photons that hit a PMT. To combat this, a sophisticated
499 water treatment system has been developed [80, 84]. UV lights, mechanical filters, and
500 membrane degasifiers are used to reduce the bacteria, suspended particulates, and
501 radioactive materials from the water. The flow of water within the tank is also critical
502 as it can remove stagnant bacterial growth or build-up of dust on the surfaces within
503 the tank. Gravity drifts impurities in the water towards the bottom of the tank which,
504 if left uncontrolled, can create asymmetric water conditions between the top and
505 bottom of the tank. Typically, the water entering the tank is cooled below the ambient
506 temperature of the tank to control convection and inhibit bacteria growth. Furthermore,
507 the dark noise hits within PMTs is sensitive to the PMT temperature [85] so controlling
508 the temperature gradients within the tank is beneficial for stable measurements.

509 SK-VI is the first phase of the SK experiment to use gadolinium dopants within
510 the ultrapure water DB: [Link to Linyan's talk at Nu2022](#). As such, the SK water
511 system had to be replaced to avoid removing the gadolinium concentrate from the
512 ultrapure water [86]. For an inverse β -decay (IBD) interaction in a water target, the
513 emitted neutron is thermally captured on hydrogen. This process releases 2.2MeV γ
514 rays which are difficult to detect due to Compton scattered electrons from a γ ray of
515 this energy is very close to the Cherenkov threshold, limiting the number of photons
516 produced. Thermal capture of neutrons on gadolinium generates γ rays with higher
517 energy meaning they are more easily detected. SK-VI has 0.01% Gd loading (0.02%
518 gadolinium sulphate by mass) which causes $\approx 50\%$ of neutrons emitted by IBD to
519 be captured on gadolinium [87, 88]. Whilst predominantly useful for low energy
520 analyses, Gd loading allows better $\nu/\bar{\nu}$ separation for atmospheric neutrino event
521 selections [89]. Efforts are currently in place to increase the gadolinium concentrate to
522 0.03% for $\approx 75\%$ neutron capture efficiency on gadolinium DB: [Link to Mark's talk at](#)
523 [Nu2022](#). The final stage of loading targets 0.1% concentrate.

⁵²⁴ 2.1.2 Calibration

⁵²⁵ The calibration of the SK detector is documented in [79] and summarised below. The
⁵²⁶ analysis presented within this thesis is dependent upon ‘high energy events’ (Charged
⁵²⁷ particles with $O(> 100)\text{MeV}$ momenta). These are events that are expected to generate
⁵²⁸ a larger number of photons such that each PMT will be hit with multiple photons.
⁵²⁹ The reconstruction of these events depends upon the charge deposited within each
⁵³⁰ PMT and the timing response of each individual PMT. Therefore, the most relevant
⁵³¹ calibration techniques to this thesis are outlined.

⁵³² Before installation, 420 PMTs were calibrated to have identical charge responses
⁵³³ and then distributed throughout the tank in a cross-shape pattern (As illustrated by
⁵³⁴ Figure 2.2). These are used as a standardised measure for the rest of the PMTs installed
⁵³⁵ at similar geometric positions within SK to be calibrated against. To perform this
⁵³⁶ calibration, a xenon lamp is located at the center of the SK tank which flashes uniform
⁵³⁷ light at 1Hz. This allows for geometrical effects, water quality variation, and timing
⁵³⁸ effects to be measured in-situ throughout normal data-taking periods.

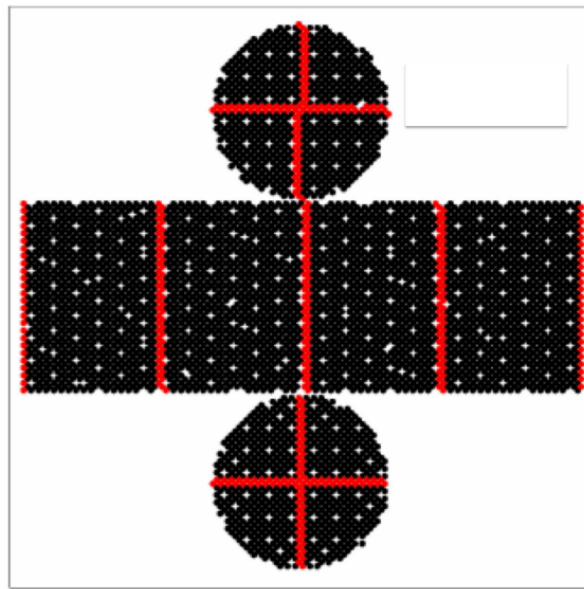


Figure 2.2: The location of “standard PMTs” (red) inside the SK detector. Taken from [79].

⁵³⁹ When specifically performing calibration of the detector (in out-of-data taking
⁵⁴⁰ mode), the water in the tank was circulated to avoid top/bottom asymmetric water
⁵⁴¹ quality. Any non-uniformity within the tank significantly affects the PMT hit proba-
⁵⁴² bility through scattering or absorption. This becomes a dominant effect for the very

543 low-intensity light sources discussed later which are designed such that only one
 544 photon is incident upon a given PMT.

545 The “gain” of a PMT is defined as the ratio of the total charge of the signal produced
 546 compared to the charge of photoelectrons emitted by the photocathodes within the
 547 PMT. To calibrate the signal of each PMT, the “relative” and “absolute” gain values are
 548 measured. The relative gain is the variation of gain among each of the PMTs whereas
 549 the absolute gain is the average gain of all PMTs.

550 The relative gain is calibrated as follows. A laser is used to generate two measure-
 551 ments; a high-intensity flash that illuminates every PMT with a sufficient number of
 552 photons, and a low-intensity flash in which only a small number of PMTs collect light.
 553 The first measurement creates an average charge, $Q_{obs}(i)$ on PMT i , whereas the second
 554 measurement ensures that each hit PMT only generates a single photoelectron. For the
 555 low-intensity measurement, the number of times each PMT records a charge larger
 556 than 1/4 photoelectrons, $N_{obs}(i)$, is counted. The values measured can be expressed as

$$\begin{aligned} Q_{obs}(i) &\propto I_H \times f(i) \times \epsilon(i) \times G(i), \\ N_{obs}(i) &\propto I_L \times f(i) \times \epsilon(i), \end{aligned} \quad (2.1)$$

557 Where I_H and I_L is the intensity of the high and low flashes, $f(i)$ is the acceptance
 558 efficiency of the i^{th} PMT, $\epsilon(i)$ is the product of the quantum and collection efficiency
 559 of the i^{th} PMT and $G(i)$ is the gain of the i^{th} PMT. The relative gain for each PMT can
 560 determined by taking the ratio of these quantities.

561 The absolute gain calibration is performed by observing fixed energy γ -rays of
 562 $E_\gamma \sim 9\text{MeV}$ emitted isotropically from neutron capture on a NiCf source situated at
 563 the center of the detector. This generates a photon yield of about 0.004 photoelec-
 564 trons/PMT/event, meaning that $> 99\%$ of PMT signals are generated from single
 565 photoelectrons. A charge distribution is generated by performing this calibration over
 566 all PMTs, and the average value of this distribution is taken to be the absolute gain
 567 value.

568 As mentioned in subsection 2.1.1, the average quantum and collection efficiency
 569 for the SK detector is $\sim 21\%$ and $> 70\%$ respectively. However, these values do differ
 570 between each PMT and need to be calibrated accordingly. Consequently, the NiCf
 571 source is also used to calibrate the “quantum \times collection” efficiency (denoted “QE”)

572 value of each PMT. The NiCf low-intensity source is used as the PMT hit probability
573 is proportional to the QE ($N_{obs}(i) \propto \epsilon(i)$ in Equation 2.1). A Monte Carlo prediction
574 which includes photon absorption, scattering, and reflection is made to estimate the
575 number of photons incident on each PMT and the ratio of the number of predicted
576 to observed hits is calculated. The difference is attributed to the QE efficiency of that
577 PMT. This technique is extended to calculate the relative QE efficiency by normalizing
578 the average of all PMTs which removes the dependence on the light intensity.

579 Due to differing cable lengths and readout electronics, the timing response between
580 a photon hitting the PMT and the signal being captured by the data acquisition can be
581 different between each PMT. Due to threshold triggers (Described in subsection 2.1.3),
582 the time at which a pulse reaches a threshold is dependent upon the size of the pulse.
583 This is known as the ‘time-walk’ effect and also needs to be accounted for in each PMT.
584 To calibrate the timing response, a pulse of light with width 0.2ns is emitted into the
585 detector through a diffuser Two-dimensional distributions of time and pulse height
586 (or charge) are made for each PMT and are used to calibrate the timing response. This
587 is performed in-situ whilst data taking with the light source pulsing at 0.03Hz.

588 The top/bottom water quality asymmetry is measured using the NiCf calibration
589 data and cross-referencing these results to the “standard PMTs”. The water attenuation
590 length is continuously measured by the rate of vertically-downgoing cosmic-ray
591 muons which enter via the top of the tank.

592 2.1.3 Data Acquisition and Triggering

593 Dark noise is the phenomenon where a PMT registers a pulse that is consistent with a
594 single photoelectron emitted from photon detection despite the PMT being in complete
595 darkness. This is predominately caused by two processes. Firstly there is intrinsic
596 dark noise which is where photoelectrons gain enough thermal energy to be emitted
597 from the photocathode, and secondly, the radioactive decay of contaminants inside the
598 structure of the PMT. Typical dark noise rate for PMTs used within SK are $O(3)\text{kHz}$ [80]
599 which equates to about 12 dark noise hits per 220ns [90]. This is lower than the
600 expected number of photons generated for a ‘high energy event’ (As described in
601 subsection 2.1.4) but instability in this value can cause biases in reconstruction.

602 The analysis presented in this thesis only uses the SK-IV period of the SK exper-
603 iment so this subsection focuses on the relevant points of the data acquisition and

triggering systems to that SK period. The earlier data acquisition and triggering systems are documented in [91, 92].

Before the SK-IV period started, the existing front-end electronics were replaced with “QTC-Based Electrons with Ethernet, QBEE” systems [93]. When the QBEE observes a signal above a 1/4 photoelectron threshold, the charge-to-time (QTC) converter generates a rectangular pulse. The start of the rectangular pulse indicates the time at which the analog photoelectron signal was received and the width of the pulse indicates the total charge integrated throughout the signal. This is then digitized by time-to-digital converters and sent to the “front-end” PCs. The digitized signal from every QBEE is then chronologically ordered and sent to the “merger” PCs. It is the merger PCs that apply the software trigger. Any triggered events are passed to the “organizer” PC. This sorts the data stream of multiple merger PCs into chronologically ordered events which are then saved to disk. The schematic of data flow from PMTs to disk is illustrated in Figure 2.3.

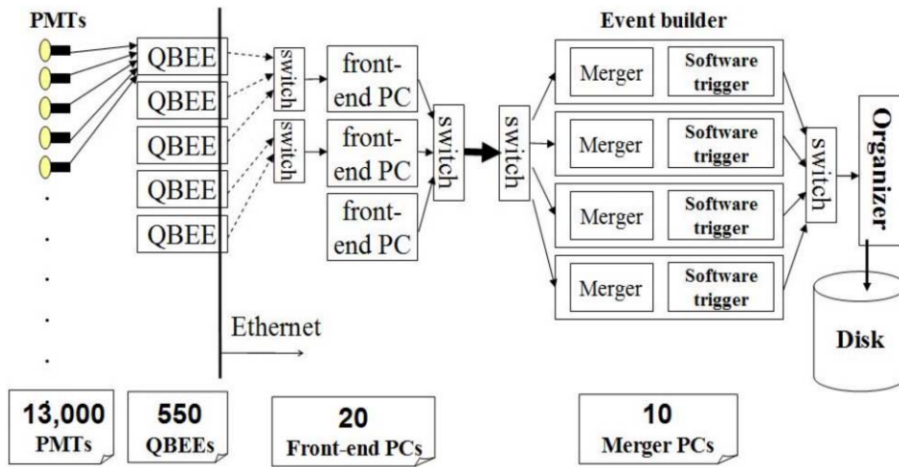


Figure 2.3: Schematic view of the data flow through the data acquisition and online system. Taken from [94].

The software trigger (described in [95]) operates by determining the number of PMT hits within a 200ns sliding window, N_{200} , coincides with the maximum time that a Cherenkov photon would take to traverse the length of the SK tank [92]. For lower energy events that generate fewer photons, this technique is useful for eliminating background processes like dark noise and radioactive decay which would be expected to separate in time. When the value of N_{200} exceeds some threshold, a software trigger is issued. There are several trigger thresholds used within the SK-IV period which are detailed in Table 2.2. If one of these thresholds is met, the PMT hits within an extended

time window are also read out and saved to disk. In the special case of an event that exceeds the SHE trigger but does not exceed the OD trigger, the AFT trigger looks for delayed coincidences of 2.2MeV gamma rays emitted from neutron capture in a $535\mu\text{s}$ window after the SHE trigger. A similar but more complex “Wideband Intelligent Trigger (WIT)” has been deployed and is described in [90].

Trigger	Acronym	Condition	Extended time window (μs)
Super Low Energy	SLE	>34/31 hits	1.3
Low Energy	LE	>47 hits	40
High Energy	HE	>50 hits	40
Super High Energy	SHE	>70/58 hits	40
Outer Detector	OD	>22 hits in OD	N/A

Table 2.2: The trigger thresholds and extended time windows saved around an event which were utilised throughout the SK-IV period. The exact thresholds can change and the values listed here represent the thresholds at the start and end of the SK-IV period.

2.1.4 Cherenkov Radiation

Cherenkov light is emitted from any highly energetic charged particle traveling with relativistic velocity, β , greater than the local speed of light in a medium [96]. Cherenkov light is formed at the surface of a cone with characteristic pitch angle,

$$\cos(\theta) = \frac{1}{\beta n}. \quad (2.2)$$

where n is the refractive index of the medium. Consequently, the Cherenkov momentum threshold, P_{thres} , is dependent upon the mass, m , of the charged particle moving through the media,

$$P_{thres} = \frac{m}{\sqrt{n^2 - 1}} \quad (2.3)$$

For water, where $n = 1.33$, the Cherenkov threshold momentum and energy for various particles are given in Table 2.3. In contrast, γ -rays are detected indirectly via

the combination of photons generated by Compton scattering and pair production. The threshold for detection in the SK detector is typically higher than the threshold for photon production. This is due to the fact that the attenuation of photons in the water means that typically $\sim 75\%$ of Cherenkov photons reach the ID PMTs. Then the collection and quantum efficiencies described in subsection 2.1.1 result in the number of detected photons being lower than the number of photons which reach the PMTs.

Particle	Threshold Momentum (MeV)	Threshold Energy (MeV)
Electron	0.5828	0.7751
Muon	120.5	160.3
Pion	159.2	211.7
Proton	1070.0	1423.1

Table 2.3: The threshold momentum and energy for a particle to generate Cherenkov light in ultrapure water, as calculated in Equation 2.2 in ultrapure water which has refractive index $n = 1.33$.

The Frank-Tamm equation [97] describes the relationship between the number of Cherenkov photons generated per unit length, dN/dx , the wavelength of the photons generated, λ , and the relativistic velocity of the charged particle,

$$\frac{d^2N}{dxd\lambda} = 2\pi\alpha \left(1 - \frac{1}{n^2\beta^2}\right) \frac{1}{\lambda^2}. \quad (2.4)$$

where α is the fine structure constant. For a 100MeV momentum electron, approximately 330 photons will be produced per centimeter in the $300\text{nm} \leq \lambda \leq 700\text{nm}$ region which the ID PMTs are most sensitive to [80].

2.2 The Tokai to Kamioka Experiment

The Tokai to Kamioka (T2K) experiment is a long-baseline neutrino oscillation experiment located in Japan. Proposed in the early 2000s [98, 99] to replace K2K [100], T2K was designed to observe electron neutrino appearance whilst precisely measuring the oscillation parameters associated with muon neutrino disappearance [101]. The experiment consists of a neutrino beam generated at the Japan Proton Accelerator Research Complex (J-PARC), a suite of near detectors situated 280m from the beam

target, and the Super Kamiokande far detector positioned at a 295km baseline. The cross-section view of the T2K experiment is drawn in Figure 2.4.

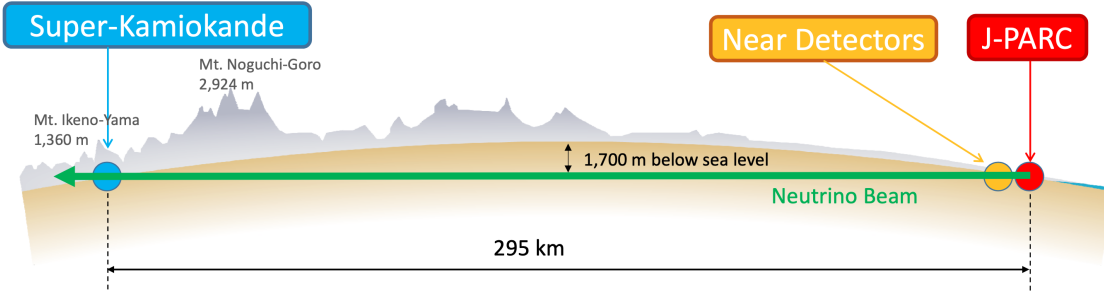


Figure 2.4: The cross-section view of the Tokai to Kamioka experiment illustrating the beam generation facility at J-PARC, the near detector situated at a baseline of 280m and the Super Kamiokande far detector situated 295km from the beam target.

The T2K collaboration makes world-leading measurements of the $\sin^2(\theta_{23})$, Δm_{23}^2 , and δ_C oscillation parameters. Improvements in the precision and accuracy of parameter estimates are still being made by including new data samples and developing the models which describe the neutrino interactions and detector responses DB: [Link to Christophe's slides from Nu2022](#). Electron neutrino appearance was first observed at T2K in 2014 [102] which accompanied a 7.3σ significance of a non-zero $\sin^2(\theta_{13})$ measurement.

The near detectors provide constraints on the beam flux and cross-section model parameters used within the fit by observing the unoscillated neutrino beam. There are a host of detectors situated in the near detector hall (As illustrated in Figure 2.5); ND280 (subsection 2.2.2), INGRID (subsection 2.2.3), NINJA [103], WAGASCI [104], and Baby-MIND [105]. The latter three are not currently used within the oscillation analysis presented within this thesis.

Whilst this thesis presents the ND280 in terms of its purpose for the oscillation analysis, the detector can also make many cross-section measurements at neutrino energies of $O(1)\text{GeV}$ for the different targets within the detector [106, 107]. These measurements are of equal importance as they can lead the way in determining the model parameters used in the interaction models for the future high-precision era of neutrino physics.

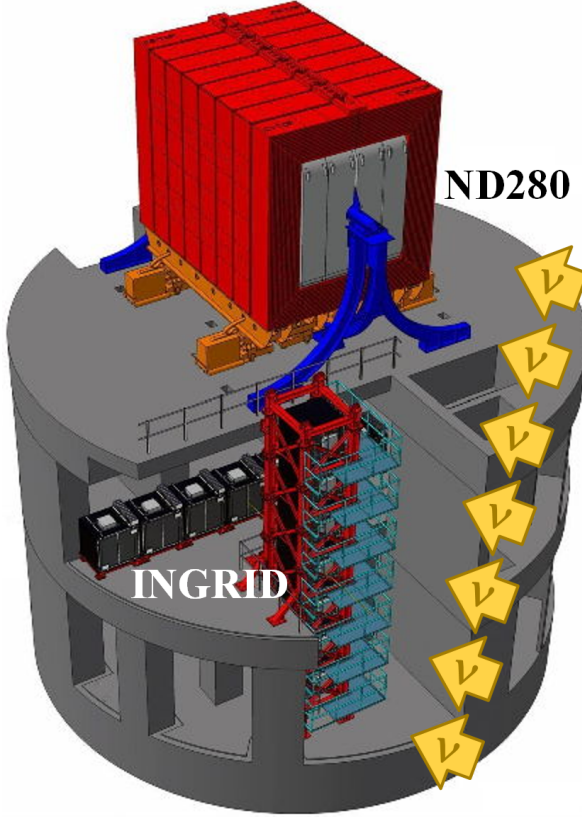
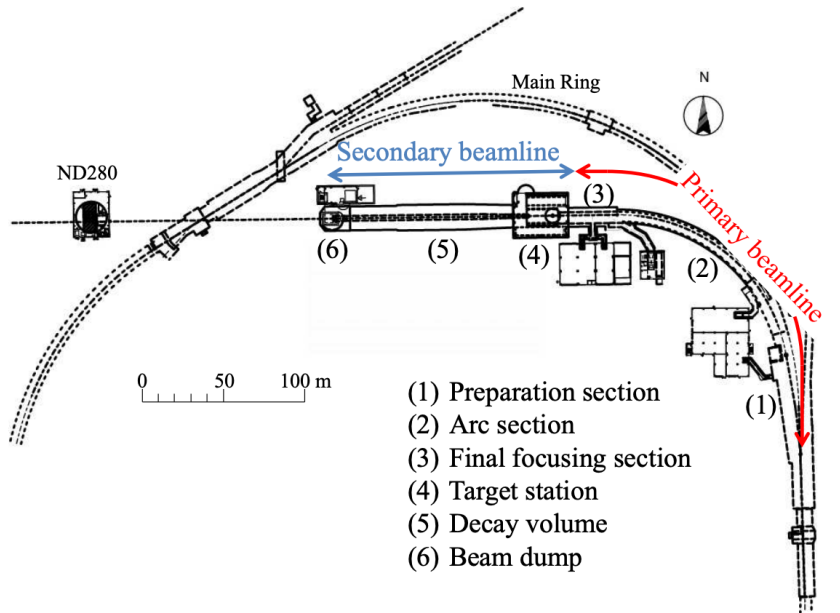


Figure 2.5: The near detector suite for the T2K experiment showing the ND280 and INGRID detectors. The distance between the detectors and the beam target is 280m.

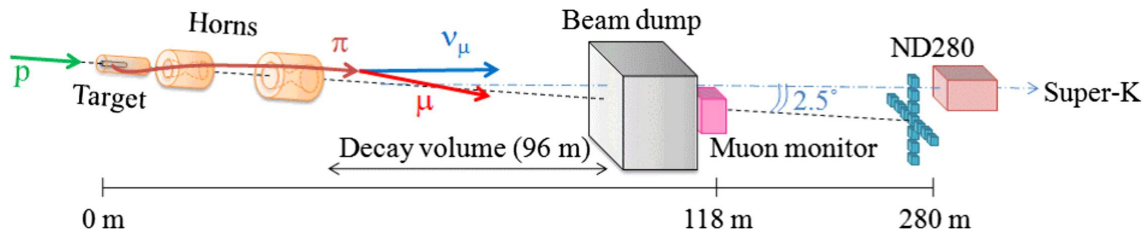
680 2.2.1 The Neutrino Beam

681 The neutrino beam used within the T2K experiment is described in [57, 108] and
 682 summarised below. The accelerating facility at J-PARC is composed of two sections; the
 683 primary and secondary beamlines. Figure 2.6 illustrates a schematic of the beamline,
 684 focusing mostly on the components of the secondary beamline. The primary beamline
 685 has three accelerators that progressively accelerate protons; a linear accelerator, a rapid-
 686 cycling synchrotron, and the main-ring (MR) synchrotron. Once fully accelerated by
 687 the MR, the protons have a kinetic energy of 30GeV. Eight bunches of these protons,
 688 separated by 500ns, are extracted per “spill” from the MR and directed towards a
 689 graphite target (A rod of length 91.4cm and diameter 2.6cm). Spills are extracted at
 690 0.5Hz with $\sim 3 \times 10^{14}$ protons contained per spill.

691 The secondary beamline consists of three main components; the target station, the
 692 decay volume, and the beam dump. The target station is comprised of the target, beam
 693 monitors, and three magnetic focusing horns. The proton beam interacts with the
 694 graphite target to form a secondary beam of mostly pions and kaons. The secondary



(a) Primary and secondary beamline



(b) Secondary beamline

Figure 2.6: Top panel: Bird's eye view of the most relevant part of primary and secondary beamline used within the T2K experiment. The primary beamline is the main-ring proton synchrotron, kicker magnet, and graphite target. The secondary beamline consists of the three focusing horns, decay volume, and beam dump. Figure taken from [108]. Bottom panel: The side-view of the secondary beamline including the focusing horns, beam dump and neutrino detectors. Figure taken from [109].

beam travels through a 96m long decay volume, generating neutrinos through the following decays [57],

$$\begin{aligned}
& \pi^+ \rightarrow \mu^+ + \nu_\mu & \pi^- \rightarrow \mu^- + \bar{\nu}_\mu \\
& K^+ \rightarrow \mu^+ + \nu_\mu & K^- \rightarrow \mu^- + \bar{\nu}_\mu \\
& \rightarrow \pi^0 + e^+ + \nu_e & \rightarrow \pi^0 + e^- + \bar{\nu}_e \\
& \rightarrow \pi^0 + \mu^+ + \nu_\mu & \rightarrow \pi^0 + \mu^- + \bar{\nu}_\mu \\
& K_L^0 \rightarrow \pi^- + e^+ + \nu_e & K_L^0 \rightarrow \pi^+ + e^- + \bar{\nu}_e \\
& \rightarrow \pi^- + \mu^+ + \nu_\mu & \rightarrow \pi^+ + \mu^- + \bar{\nu}_\mu \\
& \mu^+ \rightarrow e^+ + \bar{\nu}_\mu + \nu_e & \mu^- \rightarrow e^- + \nu_\mu + \bar{\nu}_e
\end{aligned}$$

697 The electrically charged component of the secondary beam is focused towards the
 698 far detector by the three magnetic horns. These horns direct charged particles of a
 699 particular polarity towards SK whilst defocusing the oppositely charged particles.
 700 This allows a mostly neutrino or mostly antineutrino beam to be used within the
 701 experiment, denoted as “forward horn current (FHC)” or “reverse horn current (RHC)”
 702 respectively.

703 Figure 2.7 illustrates the different contributions to the FHC and RHC neutrino flux.
 704 The low energy flux is dominated by the decay of pions whereas kaon decay becomes
 705 the dominant source of neutrinos for $E_\nu > 3\text{GeV}$. The “wrong-sign” component, which
 706 is the $\bar{\nu}_\mu$ background in a ν_μ beam, and the intrinsic irreducible ν_e background are
 707 predominantly due to muon decay for $E_\nu < 2\text{GeV}$. As the antineutrino cross-section is
 708 smaller than the neutrino cross-section, the wrong-sign component is more dominant
 709 in the RHC beam as compared to that in the FHC beam.

710 The beam dump, situated at the end of the decay volume, stops all charged particles
 711 other than highly energetic muons ($p_\mu > 5\text{GeV}$). The MuMon detector monitors the
 712 penetrating muons to determine the beam direction and intensity which is used to
 713 constrain some of the beam flux systematics within the analysis [109, 111].

714 The T2K experiment uses an off-axis beam to narrow the neutrino energy distribution.
 715 This was the first implementation of this technique in a long-baseline neutrino
 716 oscillation experiment after its original proposal [112]. Pion decay, $\pi \rightarrow \mu + \nu_\mu$, is a
 717 two-body decay. Consequently, the neutrino energy, E_ν , can be determined based on
 718 the pion energy, E_π , and the angle at which the neutrino is emitted, θ ,

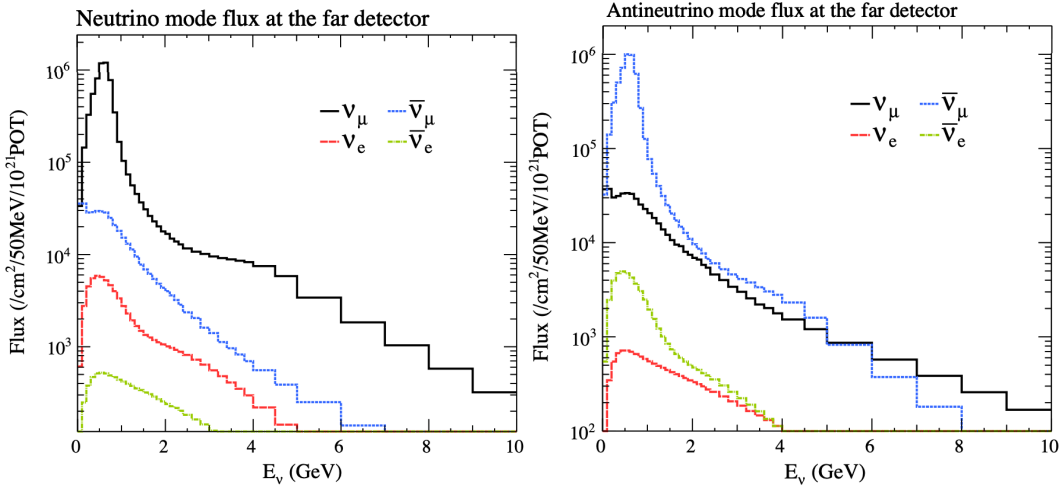


Figure 2.7: The Monte Carlo prediction of the energy spectrum for each flavour of neutrino (ν_e , $\bar{\nu}_e$, ν_μ and $\bar{\nu}_\mu$) in the neutrino dominated beam FHC mode (Left) and antineutrino dominated beam RHC mode (Right) expected at SK. Taken from [110].

$$E_\nu = \frac{m_\pi^2 - m_\mu^2}{2(E_\pi - p_\pi \cos(\theta))}, \quad (2.5)$$

where m_π and m_μ are the mass of the pion and muon respectively. For a fixed energy pion, the neutrino energy distribution is dependent upon the angle at which the neutrinos are observed from the initial pion beam direction. For the 295km baseline at T2K, $E_\nu = 0.6\text{GeV}$ maximises the electron neutrino appearance probability, $P(\nu_\mu \rightarrow \nu_e)$, whilst minimising the muon disappearance probability, $P(\nu_\mu \rightarrow \nu_\mu)$. Figure 2.8 illustrates the neutrino energy distribution for a range of off-axis angles, as well as the oscillation probabilities most relevant to T2K.

2.2.2 The Near Detector at 280m

Whilst all the near detectors are situated in the same “pit” located at 280m from the beamline, the “ND280” detector is the off-axis detector which is situated at the same off-axis angle as the Super-Kamiokande far detector. It has two primary functions; firstly it measures the neutrino flux and secondly it counts the event rates of different types of neutrino interactions. Both of these constrain the flux and cross-section systematics invoked within the model for a more accurate prediction of the expected event rate at the far detector.

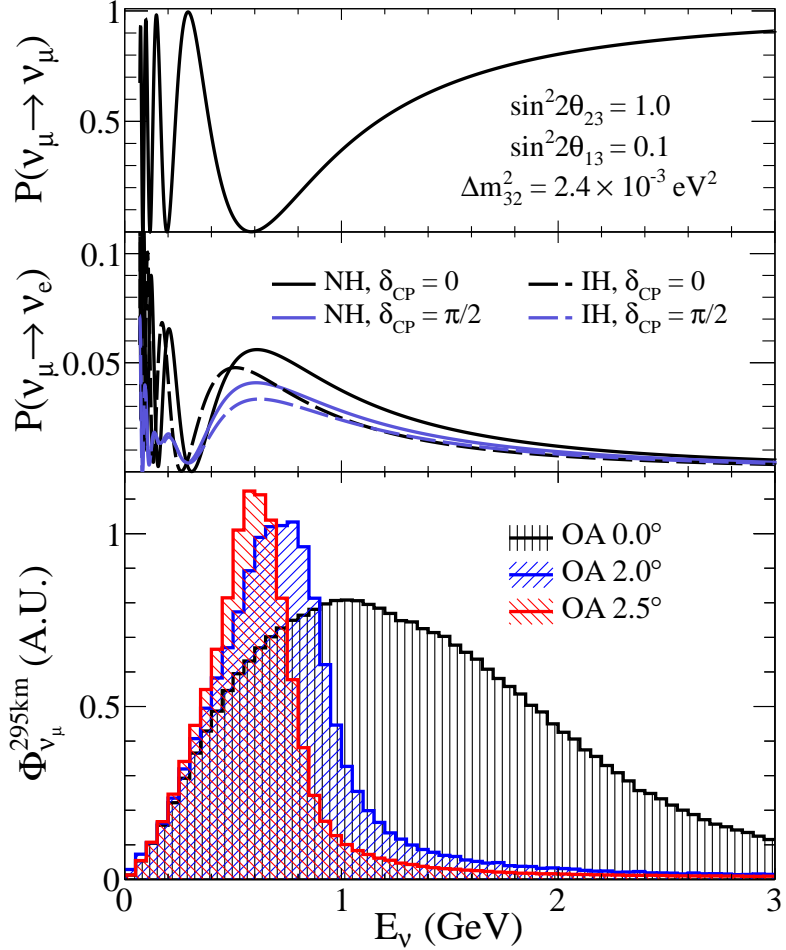


Figure 2.8: Top panel: T2K muon neutrino disappearance probability as a function of neutrino energy. Middle panel: T2K electron neutrino appearance probability as a function of neutrino energy. Bottom panel: The neutrino flux distribution for three different off-axis angles (Arbitrary units) as a function of neutrino energy.

As illustrated in Figure 2.9, the ND280 detector consists of several sub-detectors.

The most important part of the detector for this analysis is the tracker region. This is comprised of two time projection chambers (TPCs) sandwiched between three fine grain detectors (FGDs). The FGDs contain both hydrocarbon plastics and water targets for neutrino interactions and provide track reconstruction near the interaction vertex. The emitted charged particles can then propagate into the TPCs which provide particle identification and momentum reconstruction. The FGDs and TPCs are further described in subsubsection 2.2.2.1 and subsubsection 2.2.2.2 respectively. The electromagnetic calorimeter (ECAL) encapsulates the tracker region alongside the π^0 detector (P0D). The ECAL measures the deposited energy from photons emitted from interactions within the FGD. The P0D constrains the cross-section of neutral current interactions which generate neutral pions, which is one of the largest backgrounds in

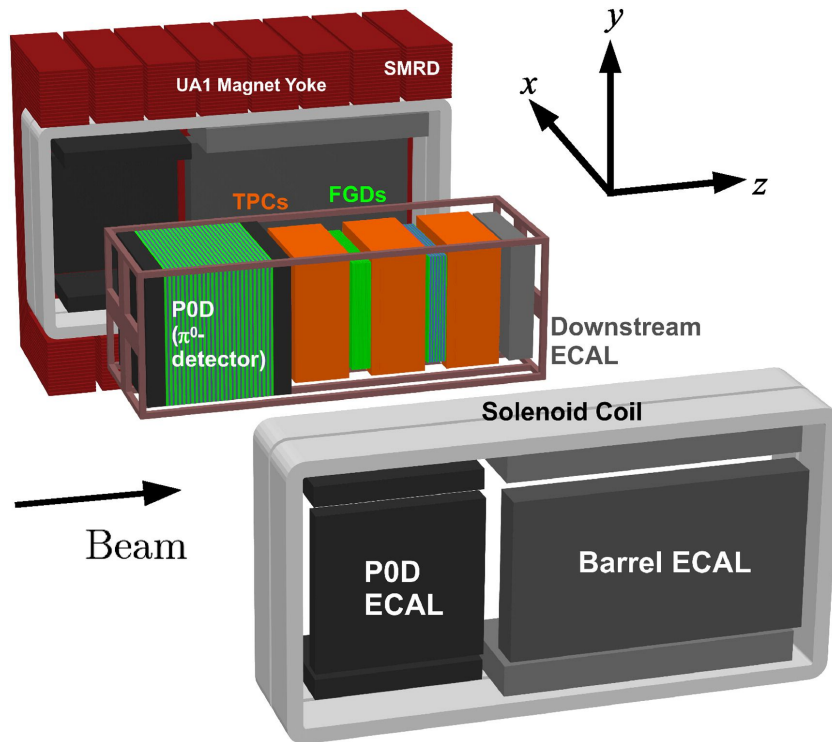


Figure 2.9: The components of the ND280 detector. The neutrino beam travels from left to right. Taken from [108].

747 the electron neutrino appearance oscillation channel. The P0D and ECAL detectors
 748 are detailed in subsubsection 2.2.2.3 and subsubsection 2.2.2.4 respectively. The entire
 749 detector is located within a large yolk magnet which produces a 0.2T magnetic field.
 750 This design of the magnet also includes a scintillating detector called the side muon
 751 range detector (SMRD) which is used to track high-angle muons as well as acting as a
 752 cosmic veto. The SMRD is described in subsubsection 2.2.2.5.

753 2.2.2.1 Fine Grained Detectors

754 The T2K tracker region is comprised of two fine grained detectors (FGD) and three
 755 Time Projection Chambers (TPC). A detailed description of the FGD design, construc-
 756 tion, and assembly is found in [113] and summarised below. The FGDs are the primary
 757 target for neutrino interactions with a mass of 1.1 tonnes per FGD. Alongside this,
 758 the FGDs are designed to be able to track short-range particles which do not exit the
 759 FGD. Typically, short-range particles are low momentum and are observed as tracks
 760 that deposit a large amount of energy per unit length. This means the FGD needs
 761 good granularity to resolve these particles. The FGDs have the best timing resolution
 762 ($\sim 3\text{ns}$) of any of the sub-detectors of the ND280 detector. As such, the FGDs are

763 used for time of flight measurements to determine forward going positively charged
 764 particles from backward going negatively charged particles. Finally, any tracks which
 765 pass through multiple sub-detectors are required to be track matched to the FGD.

766 Both FDGs are made from square scintillator planes of side length 186cm and width
 767 2.02cm. Each plane consists of two layers of 192 scintillator bars in an XY orientation.
 768 A wave-length shift fiber is threaded through the center of each bar and is read out by
 769 a multi-photon pixel counter (MPPC). FGD1 is the most upstream of the two FDGs
 770 and contains 15 planes of carbon plastic scintillator which is a common target in
 771 external neutrino scattering data. As the far detector is a pure water target, 7 of the 15
 772 scintillator planes in FGD2 have been replaced with a hybrid water-scintillator target.
 773 Due to the complexity of the nucleus, nuclear effects can not be extrapolated between
 774 different nuclei. Therefore having the ability to take data on one target which is the
 775 same as external data and another target which is the same as the far detector target is
 776 beneficial for reliable model parameter estimates.

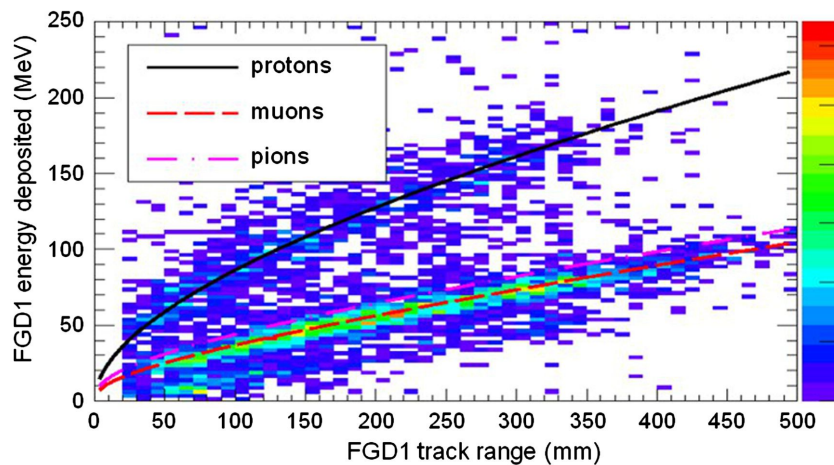


Figure 2.10: Comparison of data to Monte Carlo prediction of integrated deposited energy as a function of track length for particles that stopped in FGD1. Taken from [113].

777 The integrated deposited energy is used for particle identification. The FGD
 778 can distinguish protons from other charged particles by comparing the integrated
 779 deposited energy from data to Monte Carlo prediction as seen in Figure 2.10.

780 2.2.2.2 Time Projection Chambers

781 The majority of particle identification and momentum measurements within ND280
 782 are provided by three Time Projection Chambers (TPCs) [114]. The TPCs are located

⁷⁸³ on either side of the FGDs. They are located inside of the magnetic field meaning the
⁷⁸⁴ momentum of a charged particle can be determined from the bending of the track.

⁷⁸⁵ Each TPC module consists of two gas-tight boxes, as shown in Figure 2.11, which
⁷⁸⁶ are made of non-magnetic material. The outer box is filled with CO₂ which acts as
⁷⁸⁷ an electrical insulator between the inner box and the ground. The inner box forms
⁷⁸⁸ the field cage which produces a uniform electric drift field of $\sim 275\text{V/cm}$ and an
⁷⁸⁹ argon gas mixture. Charged particles moving through this gas mixture ionize the gas
⁷⁹⁰ mixture. The ionised charge is drifted towards micromega detectors which measure
⁷⁹¹ the ionization charge. The time and position information in the readout allows a
⁷⁹² three-dimensional image of the neutrino interaction.

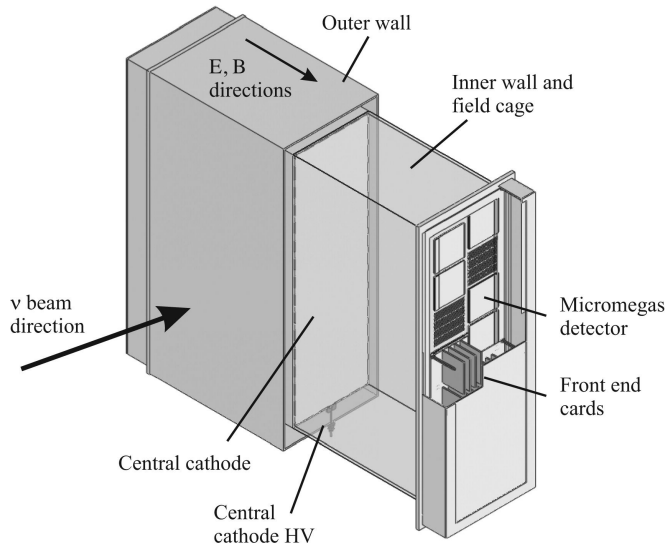


Figure 2.11: Schematic design of a Time Projection Chamber detector. Taken from [114].

⁷⁹³ The particle identification of tracks that pass through the TPCs is performed using
⁷⁹⁴ dE/dx measurements. Figure 2.12 illustrates the data to Monte Carlo distributions
⁷⁹⁵ of the energy lost by a charged particle passing through the TPC as a function of the
⁷⁹⁶ reconstructed particle momentum. The resolution is $7.8 \pm 0.2\%$ meaning that electrons
⁷⁹⁷ and muons can be distinguished. This allows reliable measurements of the intrinsic ν_e
⁷⁹⁸ component of the beam.

⁷⁹⁹ 2.2.2.3 π^0 Detector

⁸⁰⁰ If one of the γ -rays from a $\pi^0 \rightarrow 2\gamma$ decay is missed at the far detector, the reconstruc-
⁸⁰¹ tion will determine that event to be electron-like. This is one of the main backgrounds

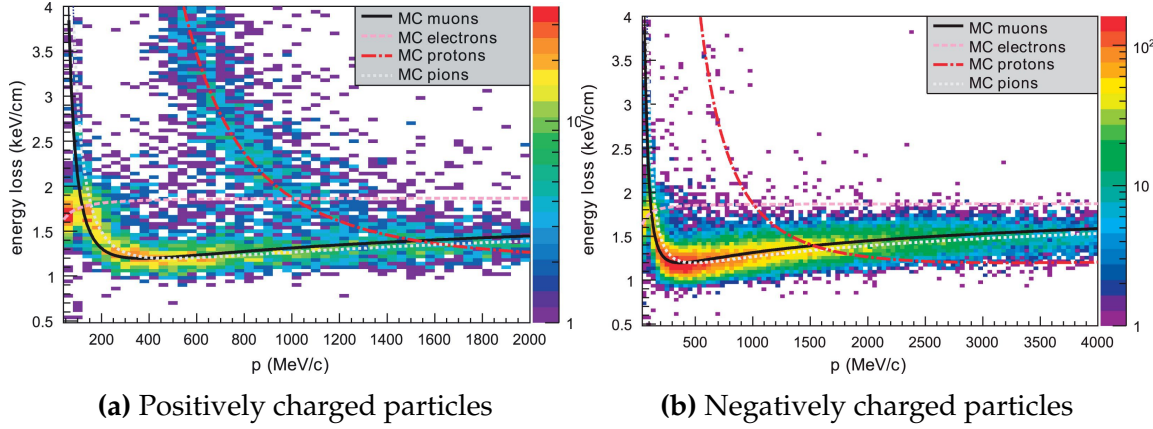


Figure 2.12: The distribution of energy loss as a function of reconstructed momentum for charged particles passing through the TPC, comparing data to Monte Carlo prediction. Taken from [114].

hindering the electron neutrino appearance searches. Therefore, the π^0 detector (P0D) measures the cross-section of the neutral current induced neutral pion production on a water target.

The P0D is a cube of approximately 2.5m length. The P0D consists of layers of scintillating bars, brass and lead sheets, and water bags as illustrated in Figure 2.13. Two electromagnetic calorimeters are positioned at the most upstream and most downstream position in the sub-detector and the water target is situated in between them. The scintillator layers are built from two triangular bars orientated in opposite directions to form a rectangular layer. Each triangular scintillator bar is threaded with optical fiber which is read out by MPPCs. The high-Z brass and lead regions produce electron showers from the photons emitted in π^0 decay.

The sub-detector can generate measurements of NC1 π^0 cross-sections on a water target by measuring the event rate both with and without the water target, with the cross-section on a water target being determined as the difference. The total active mass is 16.1 tonnes when filled with water and 13.3 tonnes when empty.

2.2.2.4 Electromagnetic Calorimeter

The electromagnetic calorimeter [116] (ECal) encapsulates the P0D and tracking sub-detectors. Its primary purpose is to aid π^0 reconstruction from any interaction in the tracker. To do this, it measures the energy and direction of photon showers from $\pi^0 \rightarrow 2\gamma$ decay. It can also distinguish pion and muon tracks depending on the shape of the photon shower deposited.

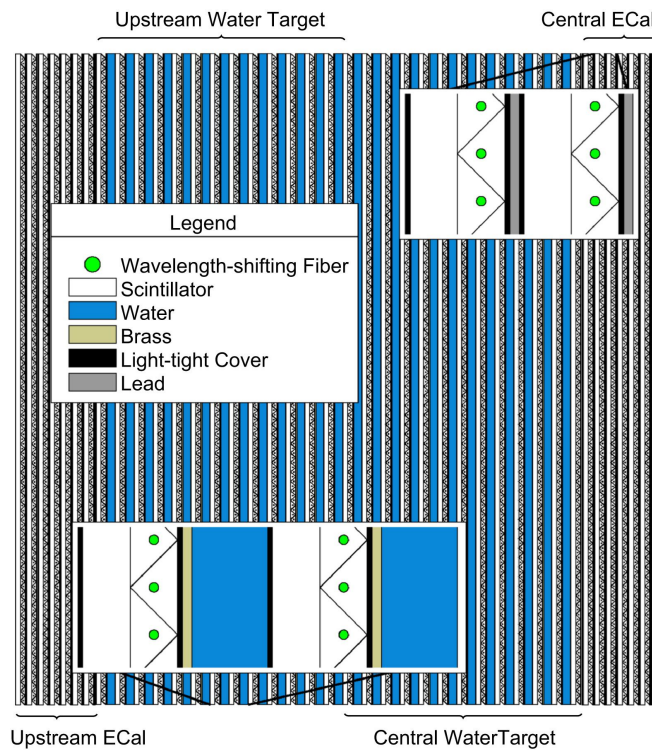


Figure 2.13: A schematic of the P0D side-view. Taken from [115].

823 The ECal is comprised of three sections; the P0D ECal which surrounds the P0D,
 824 the barrel ECal which encompasses the tracking region, and the downstream ECal
 825 which is situated downstream of the tracker region. The barrel and downstream
 826 ECals are tracking calorimeters that focus on electromagnetic showers from high-angle
 827 particles emitted from the tracking sub-detectors. Particularly in the TPC, high-angle
 828 tracks (those which travel perpendicularly to the beam-axis) can travel along a single
 829 scintillator bar resulting in very few hits. The width of the barrel and downstream
 830 ECal corresponds to ~ 11 electron radiation lengths to ensure $\sim 50\%$ of the energy of
 831 the π^0 is contained. As the P0D has its own calorimetry which reconstructs showers,
 832 the P0D ECal determines the energy which escapes the P0D.

833 Each ECal is constructed of multiple layers of scintillating bars sandwiched between
 834 lead sheets. The scintillating bars are threaded with optical fiber and read out by
 835 MPPCs. Each sequential layer of the scintillator is orientated perpendicular to the
 836 previous which allows a two-dimensional readout, which when temporal information
 837 is included results in three-dimension event displays. The target mass of the P0D ECal,
 838 barrel ECal, and downstream ECal are 1.50, 4.80 and 6.62 tonnes respectively.

839 2.2.2.5 Side Muon Range Detector

840 As illustrated in Figure 2.9, the ECal, FGDs, P0D, and TPCs are enclosed within the
 841 UA1 magnet. Originally designed for the NOMAD [117] experiment and reconditioned
 842 for use in the T2K experiment [118], the UA1 magnet provides a uniform horizontal
 843 magnetic field of $0.2 \pm 2 \times 10^{-4}$ T.

844 Built into the UA1 magnet, the side muon range detector (SMRD) [119] monitors
 845 high-energy muons which leave the tracking region and permeate through the ECal.
 846 It additionally acts as a cosmic muon veto and trigger.

847 2.2.3 The Interactive Neutrino GRID

848 The Interactive Neutrino GRID (INGRID) detector is situated within the same “pit” as
 849 the other near detectors. It is aligned with the beam in the “on-axis” position and mea-
 850 sures the beam direction, spread, and intensity. The detector was originally designed
 851 with 16 identical modules [108] (two modules have since been decommissioned) and a
 852 “proton” module. The design of the detector is cross-shaped with length and height
 853 10m × 10m as illustrated in Figure 2.14.

854 Each module is composed of iron sheets interlaced with eleven tracking scintillator
 855 planes for a total target mass of 7.1 tonnes per module. The scintillator design is an X-Y
 856 pattern of 24 bars in both orientations, where each bar contains wave-length shifting
 857 fibers which are connected to multi-pixel photon counters (MPPCs). The MPPCs
 858 convert detected photons into electrical signals via photodiodes. This is then read
 859 out by Trip-T front-end electronics [120] and passed to the readout merging modules
 860 along with timing information from the clock module. Each module is encapsulated
 861 inside veto planes to aid the rejection of charged particles entering the module.

862 The proton module is different from the other modules in that it consists of entirely
 863 scintillator planes with no iron target. The scintillator bars are also smaller than those
 864 used in the other modules to increase the granularity of the detector and improve
 865 tracking capabilities. The module sits in the center of the beamline and is designed to
 866 give precise measurements of quasi-elastic charged current interactions to evaluate
 867 the performance of the Monte Carlo simulation of the beamline.

868 The INGRID detector can measure the beam direction to an uncertainty of 0.4mrad
 869 and the beam center within a resolution of 10cm [108]. The beam direction in both the

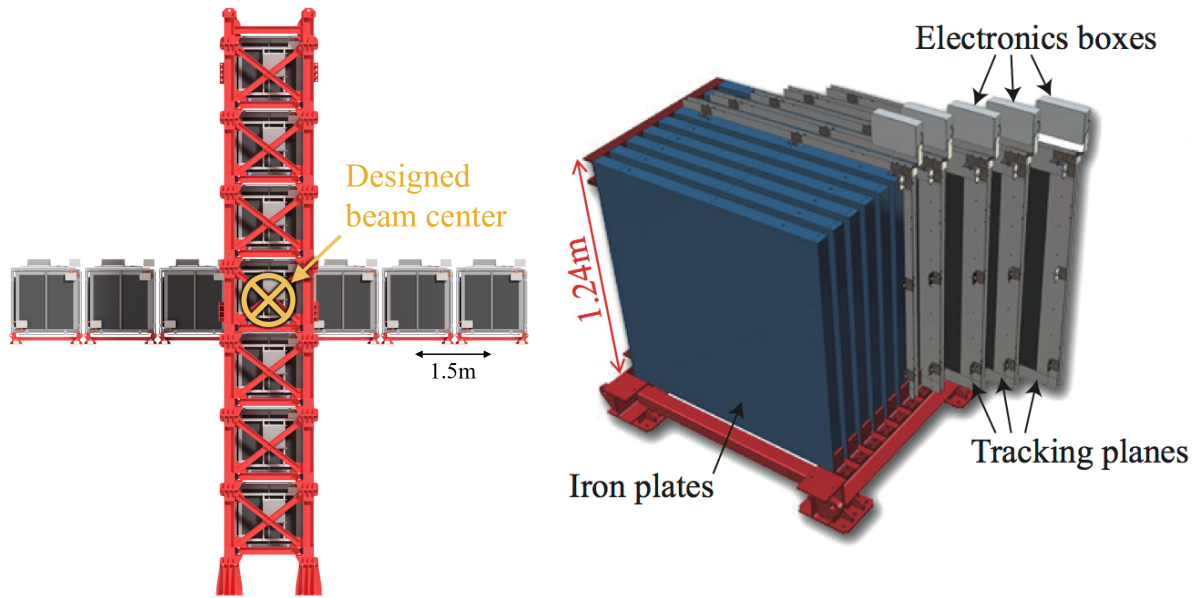


Figure 2.14: Left panel: The Interactive Neutrino GRID on-axis Detector. 14 modules are arranged in a cross-shape configuration, with the center modules being directly aligned with the on-axis beam. Right panel: The layout of a single module of the INGRID detector. Both figures are recreated from [108].

⁸⁷⁰ vertical and horizontal directions is discussed in [121] and it is found to be in good
⁸⁷¹ agreement with the MUMON monitor described in subsection 2.2.1.

872 **Chapter 3**

873 **Bayesian Statistics Implemented Through**
874 **Markov Chain Monte Carlo Techniques**

875 The analysis throughout this thesis is based upon a Bayesian oscillation analysis. To
876 extract the oscillation parameters, a Markov Chain Monte Carlo (MCMC) method is
877 used. This chapter explains the theory of how parameter estimates can be determined
878 using this technique and condenses the material found in the literature [122–125].

879 The oscillation parameter determination presented within this thesis is built upon a
880 simultaneous fit to the near detector, far detector beam, and atmospheric neutrino data.
881 In total, there are four oscillation parameters of interest ($\sin^2(\theta_{23})$, $\sin^2(\theta_{13})$, Δm_{23}^2 , and
882 δ_{CP}), two oscillation parameters to which this study will not be sensitive ($\sin^2(\theta_{12})$,
883 Δm_{12}^2) and many nuisance parameters that control the systematic uncertainty models
884 invoked within this study. The systematic uncertainties can be grouped into categories
885 depending on how they are defined; 574 bin-normalisations due to the near detector
886 response, 45 bin-normalisations to describe the far detector response to neutrino beam
887 events, 27 parameters to describe the detector response to atmospheric neutrino events,
888 100 to model the bin-normalisation due to beam flux uncertainties, 18 which model the
889 atmospheric flux uncertainties, and 87 to describe the correlated cross-section model.
890 An alternative parameterisation, where the far detector response is correlated between
891 the beam and atmospheric samples, replaces the bin-normalisation parameters with
892 224 shift and smear systematics. Section [DB: Link to Systematics Chapter](#) describes
893 the systematic model in more depth.

894 The MCMC technique generates a multi-dimensional probability distribution across
895 all of the model parameters used in the fit. To determine the parameter estimate of a
896 single parameter, this multi-dimensional object is integrated over all other parameters.
897 This process is called Marginalisation and is further described in subsection 3.3.1.
898 Monte Carlo techniques approximate the probability distribution of each parameter
899 within the limit of generating infinite samples. As ever, generating a large number of
900 samples is time and resource-dependent. Therefore, an MCMC technique is utilised

within this analysis to reduce the required number of steps to sufficiently sample the parameter space. This technique is described in further detail in subsection 3.2.1.

3.1 Bayesian Statistics

According to Bayesian Inference, observables and parameters of a statistical model are treated on an equal footing. To estimate model parameters $\vec{\theta}$ from some data D , one needs to define the joint probability distribution $P(D|\vec{\theta})$ which can be described as the prior distribution for model parameters $P(\vec{\theta})$ and the likelihood of the data given the model parameters $P(D|\vec{\theta})$,

$$P(D, \vec{\theta}) = P(D|\vec{\theta})P(\vec{\theta}). \quad (3.1)$$

The prior distribution, $P(\vec{\theta})$, describes all previous knowledge about the parameters within the model. For example, if the risk of developing health problems is known to increase with age, the prior distribution would describe the increase. For the purpose of this analysis, the prior distribution is typically the best-fit values taken from external data measurements with a Gaussian uncertainty. The prior distribution can also contain correlations between model parameters. In an analysis using Monte Carlo techniques, the likelihood of measuring some data assuming some set of model parameters is calculated by comparing the Monte Carlo prediction generated at that particular set of model parameters to the data.

It is parameter estimation that is important for this analysis and as such, we apply Bayes' theorem [126]. To calculate the probability for each parameter to have a certain value given the observed data $P(\vec{\theta}|D)$, known as the posterior distribution (often termed the posterior). This can be expressed as

$$P(\vec{\theta}|D) = \frac{P(D|\vec{\theta})P(\vec{\theta})}{\int P(D|\vec{\theta})P(\vec{\theta})d\vec{\theta}}. \quad (3.2)$$

Bayesian Statistics Implemented Through Markov Chain Monte Carlo Techniques

922 The denominator in Equation 3.2 is the integral of the joint probability distribution
923 over all values of all parameters used within the fit. For brevity, we say that the
924 posterior distribution is

$$P(\vec{\theta}|D)\alpha P(D|\vec{\theta})P(\vec{\theta}). \quad (3.3)$$

925 In subsection 3.3.1, we see that for the cases used within this analysis, it is reason-
926 able to know the posterior to some normalisation constant.

3.2 Monte Carlo Simulation

928 Monte Carlo techniques are used to numerically solve a complex problem that does
929 not necessarily have an analytical solution. These techniques rely on building a large
930 ensemble of samples from an unknown distribution and then using the ensemble to
931 approximate the properties of the distribution.

932 An example that uses Monte Carlo techniques is to calculate the area underneath
933 a curve. For example, take the problem of calculating the area under a straight line
934 with gradient $M = 0.4$ and intercept $C = 1.0$. Analytically, one can calculate the area
935 under the line is equal to 30 units for $0 \leq x \leq 10$. Using Monte Carlo techniques,
936 one can calculate the area under this line by throwing many random values for the x
937 and y components of each sample and then calculating whether that point falls below
938 the line. The area can then be calculated by the ratio of points below the line to the
939 total number of samples thrown multiplied by the total area in which samples were
940 scattered. The study is shown in Figure 3.1 highlights this technique and finds the area
941 under the curve to be 29.9 compared to an analytical solution of 30.0. The deviation
942 of the numerical to analytical solution can be attributed to the number of samples
943 used in the study. The accuracy of the approximation in which the properties of the
944 Monte Carlo samples replicate those of the desired distribution is dependent on the
945 number of samples used. Replicating this study with a differing number of Monte
946 Carlo samples used in each study (As shown in Figure 3.2) highlights how the Monte
947 Carlo techniques are only accurate within the limit of a high number of samples.

Whilst the above example has an analytical solution, these techniques are just as applicable to complex solutions. Clearly, any numerical solution is only as useful as its efficiency. As discussed, the accuracy of the Monte Carlo technique is dependent upon the number of samples generated to approximate the properties of the distribution. Furthermore, if the positions at which the samples are evaluated are not ‘cleverly’ picked, the efficiency of the Monte Carlo technique significantly drops. Given the example in Figure 3.1, if the region in which the samples are scattered significantly extends passed the region of interest, many calculations will be calculated but do not add to the ability of the Monte Carlo technique to achieve the correct result. For instance, any sample evaluated at a $y \geq 5$ could be removed without affecting the final result. This does bring in an aspect of the ‘chicken and egg’ problem in that to achieve efficient sampling, one needs to know the distribution beforehand.

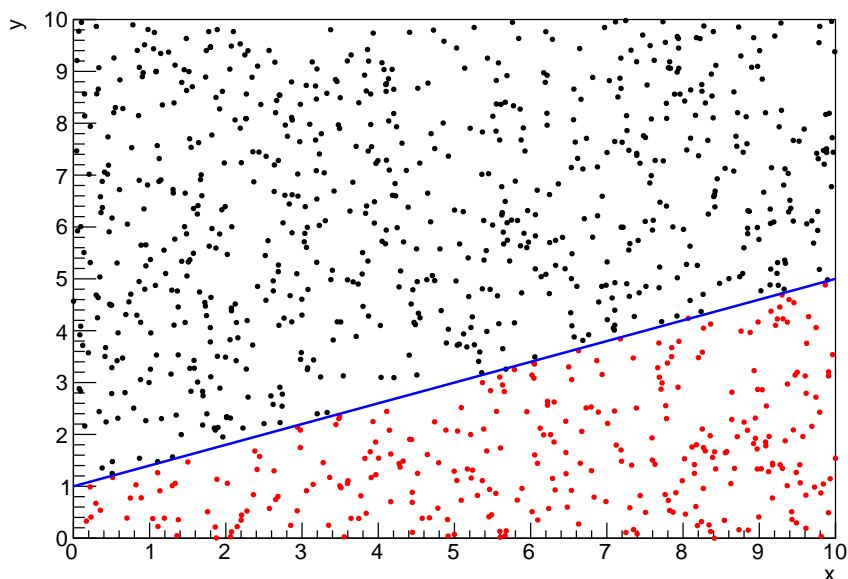


Figure 3.1: Example of using Monte Carlo techniques to find the area under the blue line. The gradient and intercept of the line are 0.4 and 1.0 respectively. The area found to be under the curve using one thousand samples is 29.9 units.

3.2.1 Markov Chain Monte Carlo

This analysis utilises a multi-dimensional probability distribution, with some dimensions being significantly more constrained than others. This could be from prior knowledge of parameter distributions from external data or un-physical regions in

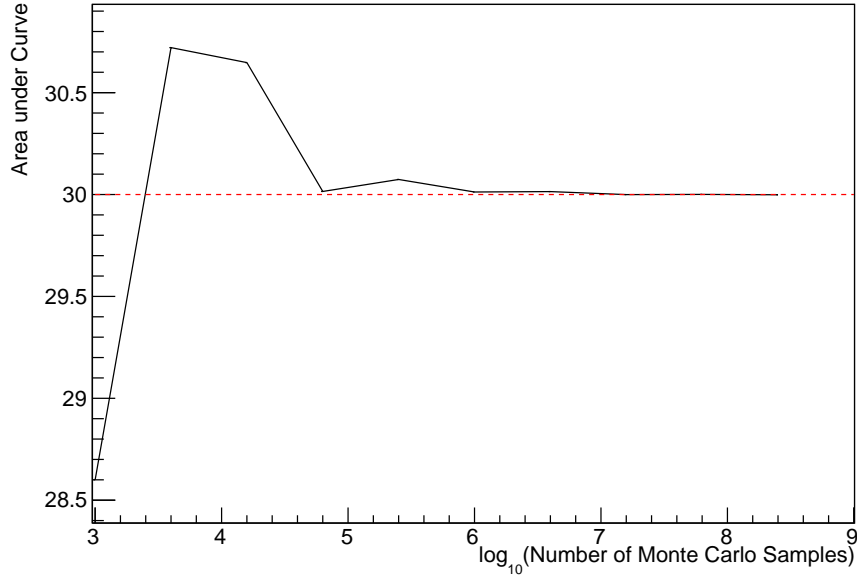


Figure 3.2: The area under a line of gradient 0.4 and intercept 1.0 for the range $0 \leq x \leq 10$ as calculated using Monte Carlo techniques as a function of the number of samples used in each repetition. The analytical solution to the area is 30 units as given by the red line.

which parameters can not exist. Consequently, the Monte Carlo techniques used need to be as efficient as possible. For this analysis, the Markov Chain Monte Carlo (MCMC) technique is chosen. An MCMC technique is a Monte Carlo technique that uses a Markov chain to select which points at which to sample the parameter distribution. This technique performs a semi-random stochastic walk through the allowable parameter space. This builds a posterior distribution which has the property that the density of sampled points is proportional to the probability density of that parameter. This does mean that the samples produced by this technique are not statistically independent but they will cover the space of the distribution.

A Markov chain functions by selecting the position of step \vec{x}_{i+1} based on the position of \vec{x}_i . The space in which the Markov chain selects samples is dependent upon the total number of parameters utilised within the fit, where a discrete point in this space is described by the N-dimensional space \vec{x} . In a perfectly operating Markov chain, the position of the next step depends solely on the previous step and not on the further history of the chain (\vec{x}_0, \vec{x}_1 , etc.). However, in solving the multi-dimensionality of the fit used within this analysis, each step becomes correlated with several of the steps preceding itself. This behaviour is further explained in subsection 3.2.3. Providing the MCMC chain is well optimised, it will begin to converge towards a

unique stationary distribution. The period between the chain's initial starting point and the convergence to the unique stationary distribution is colloquially known as the burn-in period. This is discussed further in subsection 3.2.3. Once the chain reaches the stationary distribution, all points sampled after that point will look like samples from that distribution.

Further details of the theories underpinning MCMC techniques are discussed in [123] but can be summarised by the requirement that the chain satisfies the three 'regularity conditions':

- Irreducibility: From every position in the parameter space \vec{x} , there must exist a non-zero probability for every other position in the parameter space to be reached.
- Recurrence: Once the chain arrives at the stationary distribution, every step following from that position must be samples from the same stationary distribution.
- Aperiodicity: The chain must not repeat the same sequence of steps at any point throughout the sampling period.

The output of the chain after burn-in (ie. the sampled points after the chain has reached the stationary distribution) can be used to approximate the posterior distribution and model parameters $\vec{\theta}$. To achieve the requirement that the unique stationary distribution found by the chain be the posterior distribution, one can use the Metropolis-Hastings algorithm. This guides the stochastic process depending on the likelihood of the current proposed step compared to that of the previous step. Implementation and other details of this technique are discussed in subsection 3.2.2.

3.2.2 Metropolis-Hastings Algorithm

As a requirement for MCMCs, the Markov chain implemented in this technique must have a unique stationary distribution that is equivalent to the posterior distribution. To ensure this requirement and that the regularity conditions are met, this analysis utilises the Metropolis-Hastings (MH) algorithm [127,128]. For the i^{th} step in the chain, the MH algorithm determines the position in the parameter space to which the chain moves to based on the current step, \vec{x}_i , and the proposed step, \vec{y}_{i+1} . The proposed step is randomly selected from some proposal function $f(\vec{x}_{i+1}|\vec{x}_i)$, which depends solely on the current step (ie. not the further history of the chain). The next step in the chain \vec{x}_{i+1} can be either the current step or the proposed step determined by whether the

Bayesian Statistics Implemented Through Markov Chain Monte Carlo Techniques

1013 proposed step is accepted or rejected. To decide if the proposed step is selected, the
1014 acceptance probability, $\alpha(\vec{x}_i, \vec{y}_i)$, is calculated as

$$\alpha(\vec{x}_i, \vec{y}_{i+1}) = \min \left(1, \frac{P(\vec{y}_{i+1}|D)f(\vec{x}_i|\vec{y}_{i+1})}{P(\vec{x}_i|D)f(\vec{y}_{i+1}|\vec{x}_i)} \right). \quad (3.4)$$

1015 Where $P(\vec{y}_{i+1}|D)$ is the posterior distribution as introduced in section 3.1. To
1016 simplify this calculation, the proposal function is required to be symmetric such that
1017 $f(\vec{x}_i|\vec{y}_{i+1}) = f(\vec{y}_{i+1}|\vec{x}_i)$. In practice, a multi-variate Gaussian distribution is used to
1018 throw parameter proposals from. This reduces Equation 3.4 to

$$\alpha(\vec{x}_i, \vec{y}_{i+1}) = \min \left(1, \frac{P(\vec{y}_{i+1}|D)}{P(\vec{x}_i|D)} \right). \quad (3.5)$$

1019 After calculating this quantity, a random number, β , is generated uniformly be-
1020 tween 0 and 1. If $\beta \leq \alpha(\vec{x}_i, \vec{y}_{i+1})$, the proposed step is accepted. Otherwise, the chain
1021 sets the next step equal to the current step and this procedure is repeated. This can be
1022 interpreted as if the posterior probability of the proposed step is greater than that of
1023 the current step, ($P(\vec{y}_{i+1}|D) \geq P(\vec{x}_i|D)$), the proposed step will always be accepted.
1024 If the opposite is true, ($P(\vec{y}_{i+1}|D) \leq P(\vec{x}_i|D)$), the proposed step will be accepted
1025 with probability $P(\vec{x}_i|D)/P(\vec{y}_{i+1}|D)$. This ensures that the Markov chain does not get
1026 trapped in any local minima in the potentially non-Gaussian posterior distribution.
1027 The outcome of this technique is that the density of steps taken in a discrete region is
1028 directly proportional to the probability density in that region.

1029 3.2.3 MCMC Optimisation

1030 As discussed in subsection 3.2.2, the proposal function invoked within the MH algo-
1031 rithm can take any form and the chain will still converge to the stationary distribution.
1032 As discussed in [DB: Link to Analysis Strategy Section](#), this analysis performs the
1033 Monte Carlo reweighting on an event-by-event basis. This requires significant com-
1034 putational resources to perform a parameter fit. Therefore, the number of steps taken
1035 before the unique stationary distribution is found should be minimised as only steps
1036 after convergence add information to the fit. Furthermore, the chain should entirely

1037 cover the allowable parameter space to ensure that all values have been considered.
1038 Tuning the distance that the proposal function jumps between steps on a parameter-
1039 by-parameter basis can both minimise the length of the burn-in period and ensure that
1040 the correlation between step \vec{x}_i and \vec{x}_j is sufficiently small.

1041 The effect of changing the width of the proposal function is highlighted in Figure 3.3.
1042 Three scenarios, each with the same underlying stationary distribution (A Gaussian of
1043 width 1.0 and mean 0.), are presented. The only difference between the three scenarios
1044 is the width of the proposal function, colloquially known as the ‘step size σ ’. Each
1045 scenario starts at an initial parameter value of 10.0 which would be considered an
1046 extreme variation. For the case where $\sigma = 0.1$, it is clear to see that the chain takes
1047 a long time to reach the expected region of the parameter. This indicates that this
1048 chain would have a large burn-in period and does not converge to the stationary
1049 distribution until step ~ 500 . Furthermore, whilst the chain does move towards the
1050 expected region, each step is significantly correlated with the previous. Considering
1051 the case where $\sigma = 5.0$, the chain approaches the expected parameter region almost
1052 instantly meaning that the burn-in period is not significant. However, there are clearly
1053 large regions of steps where the chain does not move. This is likely due to the chain
1054 proposing steps in the tails of the distribution which have a low probability of being
1055 accepted. Consequently, this chain would take a significant number of steps to fully
1056 span the allowable parameter region. For the final scenario, where $\sigma = 0.5$, you can see
1057 a relatively small burn-in period of approximately 100 steps. Once the chain reaches
1058 the stationary distribution, it moves throughout the expected region of parameter
1059 values many times, sufficiently sampling the full parameter region. This example is a
1060 single parameter varying across a continuous distribution and does not fully reflect
1061 the difficulties in the many-hundred multi-variate parameter distribution used within
1062 this analysis. However, it does give a conceptual idea of the importance of selecting
1063 the proposal function and associated step size.

1064 As discussed, step size tuning directly correlates to the average step acceptance
1065 rate. If the step size is too small, many steps will be accepted but the chain moves
1066 slowly. If the opposite is true, many steps will be rejected as the chain proposes steps
1067 in the tails of the distribution. Discussion in [129] suggests that the ‘ideal’ acceptance
1068 rate of a high dimension MCMC chain should be approximately $\sim 25\%$. An “ideal”
1069 step size [129] of

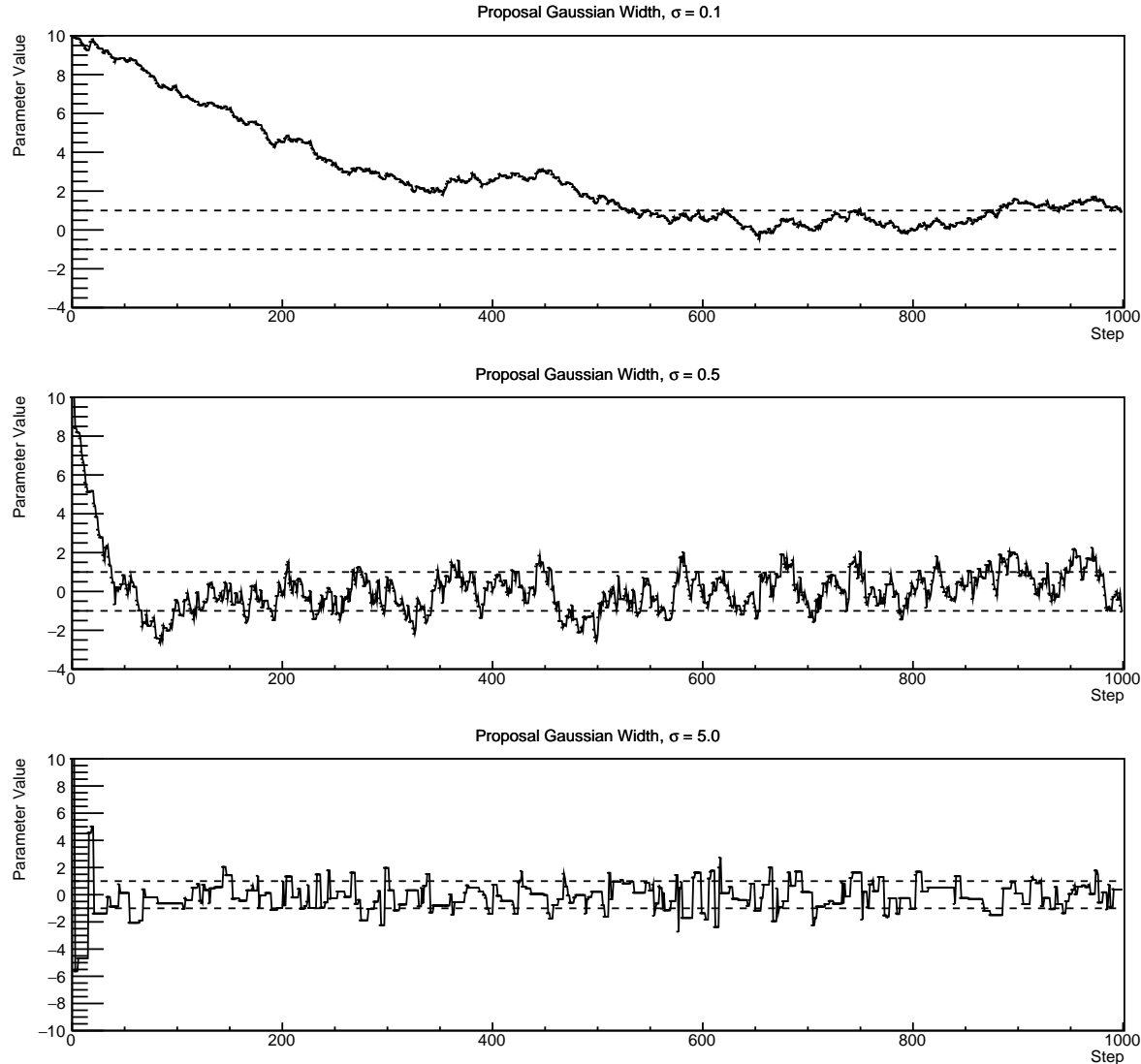


Figure 3.3: Three MCMC chains, each with a stationary distribution equal to a Gaussian centered at 0 and width 1 (As indicated by the black dotted lines). All of the chains use a Gaussian proposal function but have different widths (or ‘step size σ ’). The top panel has $\sigma = 0.1$, middle panel has $\sigma = 0.5$ and the bottom panel has $\sigma = 5.0$.

$$\sigma = \frac{2.4}{N_p}, \quad (3.6)$$

where N_p is the number of parameters included in the MCMC fit. However, the complex correlations between systematics mean that some parameters have to be hand tuned and many efforts have been taken to select a set of parameter-by-parameter step sizes to approximately reach the ideal acceptance rate.

Figure 3.3 highlights the likelihood as calculated by the fit in DB: Link to AsimovA Sensitivity Section as a function of the number of steps in each chain. In practice, many independent MCMC chains are run simultaneously to parallelise the task of performing the fit. This figure overlays the distribution found in each chain. As seen, the likelihood decreases from its initial value and converges towards a stationary distribution after $\sim 1 \times 10^5$ steps. Each fit (whether it be different asimov fits or data fit) will have a different set of preferred parameter values which results in a different stationary distribution. For each fit presented in this thesis, a burn-in period of 1×10^5 steps was found to be sufficient.

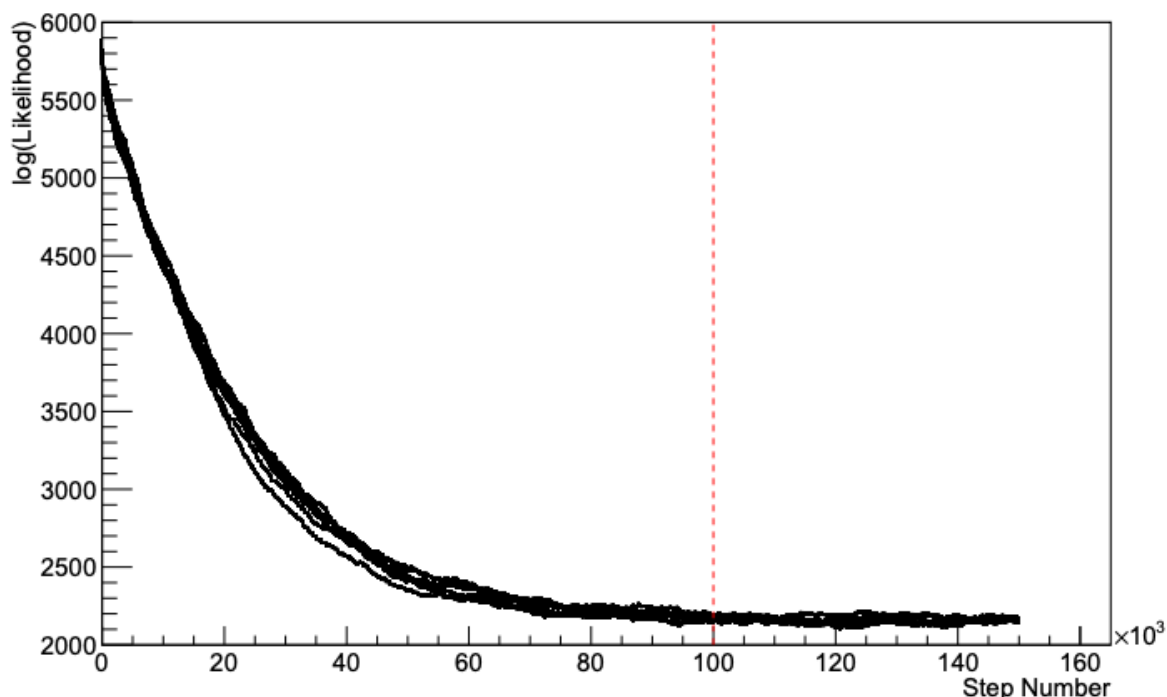


Figure 3.4: The log-likelihood from the fit detailed in DB: Link to AsimovA Sensitivity Section as a function of the number of steps accumulated in each fit. Many independent MCMC chains were run in parallel and overlaid on this plot. The red line indicates the 1×10^5 step burn-in period after which the log-likelihood becomes stable.

3.3 Understanding the MCMC Results

Whilst section 3.1 and section 3.2 describe how to interpret Bayesian statistics and explains the MCMC techniques used within this analysis, there is no mention of how to interpret the output of the chain. The posterior distribution output from the

chain is a high dimension object, with as many dimensions as there are parameters included in the fit. However, this multi-dimensional object is difficult to conceptualize so parameter estimations are often presented in one or two-dimensional projections of this probability distribution. To do this, we invoke the marginalisation technique highlighted in subsection 3.3.1.

3.3.1 Marginalisation

The output of the MCMC chain is a highly dimensional probability distribution which is very difficult to interpret. From the standpoint of an oscillation analysis experiment, the one or two-dimensional ‘projections’ of the oscillation parameters of interest are most relevant. Despite this, the best fit values and uncertainties on the oscillation parameters of interest should correctly encapsulate the correlations to the other systematic uncertainties (colloquially called ‘nuisance’ parameters). For this joint beam and atmospheric analysis, the oscillation parameters of interest are $\sin^2(\theta_{23})$, $\sin^2(\theta_{13})$, Δm_{23}^2 , and δ_{CP} . All other parameters (Including the oscillation parameter this fit is insensitive to) are deemed nuisance parameters. To generate these projections, we rely upon integrating the posterior distribution over all nuisance parameters. This is called marginalisation. A simple example of this technique is to imagine the scenario where two coins are flipped. To determine the probability that the first coin returned a ‘head’, the exact result of the second coin flip is disregarded and simply integrated over. For the parameters of interest, $\vec{\theta}_i$, we can calculate the marginalised posterior by integrating over the nuisance parameters, $\vec{\theta}_n$. In this case, Equation 3.2 becomes

$$P(\vec{\theta}_i|D) = \frac{\int P(D|\vec{\theta}_i, \vec{\theta}_n)P(\vec{\theta}_i, \vec{\theta}_n)d\vec{\theta}_n}{\int P(D|\vec{\theta})P(\vec{\theta})d\vec{\theta}} \quad (3.7)$$

Where $P(\vec{\theta}_i, \vec{\theta}_n)$ encodes the prior knowledge about the uncertainty and correlations between the parameters of interest and the nuisance parameters. In practice, this is simply taking the one or two-dimensional projection of the multi-dimensional probability distribution.

Whilst in principle an easy solution to a complex problem, correlations between the interesting and nuisance parameters can bias the marginalised results. A similar effect is found when the parameters being marginalised over have non-Gaussian probability

distributions. For example, Figure 3.5 highlights the marginalisation bias in the probability distribution found for a parameter when requiring a correlated parameter to have a positive parameter value. Due to the complex nature of this oscillation parameter fit presented in this thesis, there are certainly correlations occurring between the oscillation parameters of interest and the other nuisance parameters included in the fit.

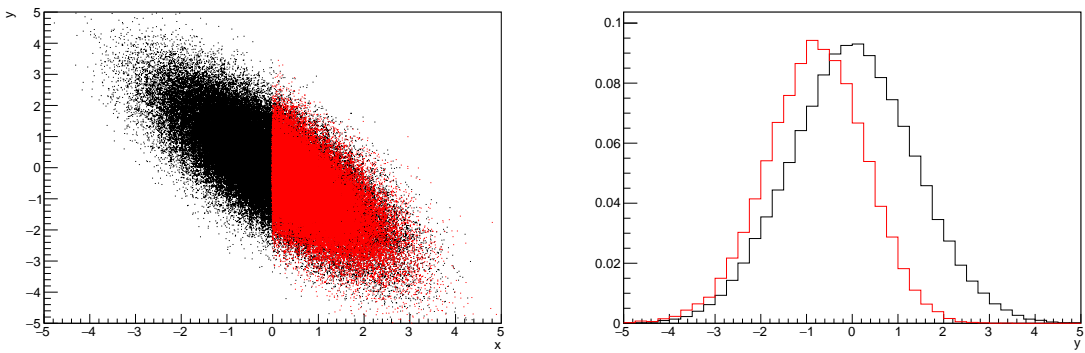


Figure 3.5: Left: The two dimensional probability distribution for two correlated parameters x and y . The red distribution shows the two dimensional probability distribution when $0 \leq x \leq 5$. Right: The marginalised probability distribution for the y parameter found when requiring the x to be bound between $-5 \leq x \leq 5$ and $0 \leq x \leq 5$ for the black and red distribution, respectively.

3.3.2 Parameter Estimation and Credible Intervals

The purpose of this analysis is to determine the best fit values for the oscillation parameters that the beam and atmospheric samples are sensitive to; $\sin^2(\theta_{23})$, $\sin^2(\theta_{13})$, Δm_{23}^2 , and δ_{CP} . Typically, the results presented take the form of one or two-dimension marginalised probability distributions for the appearance ($\sin^2(\theta_{13})$ and δ_{CP}) and disappearance ($\sin^2(\theta_{23})$ and Δm_{23}^2) parameters. The posterior probability density taken from the output MCMC chain is binned in these parameters. The parameter best-fit point is then taken to be the value that has the highest posterior probability. This is performed in both one and two-dimensional projections.

However, the single best-fit point in a given parameter is not of much use on its own. We would also like to determine the uncertainty, or credible interval, on that best-fit point. The definition of the 1σ credible interval is that we have 68% belief that the parameter is within those bounds. For a more generalised definition, the credible

Bayesian Statistics Implemented Through Markov Chain Monte Carlo Techniques

₁₁₃₄ interval is the region of the posterior distribution that contains a specific fraction of
₁₁₃₅ the total probability, such that

$$\int P(\theta|D)d\theta = \alpha \quad (3.8)$$

₁₁₃₆ Where θ is the parameter on which we calculate the credible interval. This technique
₁₁₃₇ then calculates the $\alpha \times 100\%$ credible interval.

₁₁₃₈ In practice, this analysis uses the highest posterior density (HPD) credible intervals
₁₁₃₉ which are calculated through the following method. First, the probability distribution
₁₁₄₀ is area-normalised such that it has an integrated area equal to 1.0. The bins of proba-
₁₁₄₁ bility are then summed from the highest to lowest until the sum exceeds the 1σ level
₁₁₄₂ (0.68 in this example). This process is repeated for a range of credible intervals, notably
₁₁₄₃ the 1σ , 2σ and 3σ along with other levels where the critical values for each level can
₁₁₄₄ be found in [130]. This process can be repeated for the two-dimensional probability
₁₁₄₅ distributions by creating two-dimensional contours of credible intervals rather than a
₁₁₄₆ one-dimensional result.

₁₁₄₇ 3.3.3 Application of Bayes' Theorem

₁₁₄₈ Due to the matter resonance, this analysis has some sensitivity to the mass hierarchy of
₁₁₄₉ neutrino states (whether Δm_{23}^2 is positive or negative) and the octant of $\sin^2(\theta_{23})$. The
₁₁₅₀ Bayesian approach utilised within this analysis gives an intuitive method of model
₁₁₅₁ comparison by determining which hypothesis is most favourable. Taking the ratio of
₁₁₅₂ Equation 3.3 for the two hypotheses of normal hierarchy, NH , and inverted hierarchy,
₁₁₅₃ IH , gives

$$\frac{P(\vec{\theta}_{NH}|D)}{P(\vec{\theta}_{IH}|D)} = \frac{P(D|\vec{\theta}_{NH})}{P(D|\vec{\theta}_{IH})} \times \frac{P(\vec{\theta}_{NH})}{P(\vec{\theta}_{IH})}. \quad (3.9)$$

₁₁₅₄ The middle term defines the Bayes factor which is a data-driven interpretation of
₁₁₅₅ how strong the data prefers one hierarchy to the other. For this analysis, equal priors
₁₁₅₆ on both mass hierarchy hypotheses are chosen ($P(\vec{\theta}_{NH}) = P(\vec{\theta}_{IH}) = 0.5$). In practice,

1157 the MCMC chain proposes a value of $|\Delta m_{23}^2|$ and then applies a 50% probability that
 1158 the value is sign flipped. Consequently, the Bayes factor can be calculated from the
 1159 ratio of the probability density in either hypothesis. This equates to counting the
 1160 number of steps taken in the normal and inverted hierarchies and taking the ratio. The
 1161 same approach can be taken to compare the upper octant (UO) compared to the lower
 1162 octant (LO) hypothesis of $\sin^2(\theta_{23})$.

1163 Whilst the value of the Bayes factor should always be shown, the Jeffreys scale [131]
 1164 (highlighted in Table 3.1) gives an indication of the strength of preference for one model
 1165 compared to the other. Other interpretations of the strength of preference of a model
 1166 exist, e.g. the Kass and Raferty Scale [132].

$\log_{10}(B_{AB})$	B_{AB}	Strength of Preference
< 0.0	< 1	No preference for hypothesis A (Supports hypothesis B)
0.0 – 0.5	1.0 – 3.16	Preference for hypothesis A is weak
0.5 – 1.0	3.16 – 10.0	Preference for hypothesis A is substantial
1.0 – 1.5	10.0 – 31.6	Preference for hypothesis A is strong
1.5 – 2.0	31.6 – 100.0	Preference for hypothesis A is very strong
> 2.0	> 100.0	Decisive preference for hypothesis A

Table 3.1: Jeffreys scale for strength of preference for two models A and B as a function of the calculated Bayes factor ($B_{AB} = B(A/B)$) between the two models [131]. The original scale is given in terms of $\log_{10}(B(A/B))$ but converted to linear scale for easy comparison throughout this thesis.

1167 3.3.4 Comparison of MCMC Output to Expectation

1168 Whilst not important for the extraction of oscillation parameters, understanding how
 1169 the data constrains the model parameters is important to the understanding of this
 1170 analysis. A simple method of doing this is to perform a comparison in the fitting
 1171 parameters (For instance, the reconstructed neutrino energy and lepton direction for
 1172 T2K far detector beam samples) of the spectra generated by the MCMC chain to ‘data’.
 1173 This ‘data’ could be true data or some variation of Monte Carlo prediction. This allows
 1174 easy comparison of the MCMC probability distribution to the data. To perform this, N
 1175 steps from the post burn-in MCMC chain are randomly selected (Where for all plots
 1176 of this style in this thesis, $N = 3000$). From these, the Monte Carlo prediction at each
 1177 step is generated by reweighting the model parameters to the values specified at that

Bayesian Statistics Implemented Through Markov Chain Monte Carlo Techniques

1178 step. Due to the probability density being directly correlated with the density of steps
1179 in a certain region, parameter values close to the best fit value are most likely to be
1180 selected.

1181 In practice, for each bin of the fitting parameters has a probability distribution
1182 of event rates, with one entry per sampled MCMC step. This distribution is binned
1183 where the bin with the highest probability is selected as the mean and an error on
1184 the width of this probability distribution is calculated using the approach highlighted
1185 in subsection 3.3.2. Consequently, the best fit distribution in the fit parameter is not
1186 necessarily that which would be attained by reweighting the Monte Carlo prediction
1187 to the most probable parameter values.

1188 A similar study can be performed to illustrate the freedom of the model parameter
1189 space prior to the fit. This can be done by throwing parameter values from the prior
1190 uncertainty of each parameter. This becomes troublesome for parameters with no
1191 prior uncertainty as the range is technically infinite. Where applicable solutions to
1192 remove these have been addressed.

1193

₁₁₉₄ **Bibliography**

- ₁₁₉₅ [1] J. Chadwick, Verhandl. Dtsc. Phys. Ges. **16**, 383 (1914).
- ₁₁₉₆ ₁₁₉₇ [2] C. D. Ellis and W. A. Wooster, Proc. R. Soc. Lond. A Math. Phys. Sci. **117**, 109 (1927).
- ₁₁₉₈ [3] W. Pauli, Phys. Today **31N9**, 27 (1978).
- ₁₁₉₉ [4] E. Fermi, Z. Phys. **88**, 161 (1934).
- ₁₂₀₀ [5] F. Reines and C. L. Cowan, Phys. Rev. **92**, 830 (1953).
- ₁₂₀₁ ₁₂₀₂ [6] C. L. Cowan, F. Reines, F. B. Harrison, H. W. Kruse, and A. D. McGuire, Science **124**, 103 (1956), <http://science.sciencemag.org/content/124/3212/103.full.pdf>.
- ₁₂₀₃ [7] G. Danby *et al.*, Phys. Rev. Lett. **9**, 36 (1962).
- ₁₂₀₄ [8] K. Kodama *et al.*, Physics Letters B **504**, 218 (2001).
- ₁₂₀₅ [9] LSND, A. Aguilar-Arevalo *et al.*, Phys. Rev. **D64**, 112007 (2001), hep-ex/0104049.
- ₁₂₀₆ ₁₂₀₇ [10] MiniBooNE Collaboration, A. A. Aguilar-Arevalo *et al.*, Phys. Rev. Lett. **110**, 161801 (2013).
- ₁₂₀₈ [11] and P. A. R. Ade *et al.*, Astronomy and Astrophysics **594**, A13 (2016).
- ₁₂₀₉ [12] B. Pontecorvo, Sov. Phys. JETP **26**, 984 (1968), [Zh. Eksp. Teor. Fiz. 53, 1717 (1967)].
- ₁₂₁₀ [13] B. Pontecorvo, Sov. Phys. JETP **7**, 172 (1958), [Zh. Eksp. Teor. Fiz. 34, 247 (1957)].
- ₁₂₁₁ [14] M. Kobayashi and T. Maskawa, Progress of Theoretical Physics **49**, 652 (1973).
- ₁₂₁₂ [15] N. Cabibbo, Phys. Rev. Lett. **10**, 531 (1963).
- ₁₂₁₃ [16] A. Y. Smirnov, (2003).
- ₁₂₁₄ [17] S. Mikheyev and A. Smirnov, Soviet Journal of Nuclear Physics **42**, 913 (1985).
- ₁₂₁₅ [18] L. Wolfenstein, Phys. Rev. D **17**, 2369 (1978).
- ₁₂₁₆ [19] A. M. Dziewonski and D. L. Anderson, Phys. Earth Planet. Inter. **25**, 297 (1981).
- ₁₂₁₇ ₁₂₁₈ [20] R. Wendell, *Three Flavor Oscillation Analysis of Atmospheric Neutrinos in Super-Kamiokande*, PhD thesis, University of North Carolina, 2008.

- [21] The Super-Kamiokande Collaboration, Y. Ashie *et al.*, Phys. Rev. Lett. **93**, 101801 (2004).
- [22] SNO Collaboration, Q. R. Ahmad *et al.*, Phys. Rev. Lett. **89**, 011301 (2002).
- [23] 2015 Nobel prize in Physics as listed by Nobelprize.org, https://www.nobelprize.org/nobel_prizes/physics/laureates/2015/, Accessed: 18-04-2018.
- [24] J. A. Formaggio and G. P. Zeller, Rev. Mod. Phys. **84**, 1307 (2012), 1305.7513.
- [25] A. Bellerive, Int. J. Mod. Phys. A **19**, 1167 (2004).
- [26] R. Davis, D. S. Harmer, and K. C. Hoffman, Phys. Rev. Lett. **20**, 1205 (1968).
- [27] N. Vinyoles *et al.*, Astrophys. J. **835**, 202 (2017).
- [28] V. Gribov and B. Pontecorvo, Phys. Lett. B **28**, 493 (1969).
- [29] K. S. Hirata *et al.*, Phys. Rev. Lett. **63**, 16 (1989).
- [30] W. Hampel *et al.*, Phys. Lett. B **447**, 127 (1999).
- [31] SAGE Collaboration, J. N. Abdurashitov *et al.*, Phys. Rev. C **60**, 055801 (1999).
- [32] Q. R. Ahmad *et al.*, Phys. Rev. Lett. **89** (2002).
- [33] Borexino Collaboration, Nature **562**, 505 (2018).
- [34] B. Aharmim *et al.*, Astrophys. J. **653**, 1545 (2006).
- [35] M. Agostini *et al.*, (2020).
- [36] S. Andringa *et al.*, Adv. High Energy Phys. **2016**, 1 (2016).
- [37] J. F. Beacom *et al.*, Chin. phys. C **41**, 023002 (2017).
- [38] F. An *et al.*, J. Phys. G Nucl. Part. Phys. **43**, 030401 (2016).
- [39] J. Aalbers *et al.*, (2020), 2006.03114.
- [40] T. K. Gaisser and M. Honda, (2002).
- [41] G. D. Barr, T. K. Gaisser, P. Lipari, S. Robbins, and T. Stanev, Physical Review D **70** (2004).
- [42] M. Honda, T. Kajita, K. Kasahara, S. Midorikawa, and T. Sanuki, Physical Review

- 1245 D **75** (2007).
- 1246 [43] M. Honda, T. Kajita, K. Kasahara, and S. Midorikawa, Phys. Rev. D **70**, 043008
1247 (2004).
- 1248 [44] A. Fasso, A. Ferrari, P. R. Sala, and J. Ranft, (2001).
- 1249 [45] Y. Ashie *et al.*, Physical Review D **71** (2005).
- 1250 [46] F. Reines *et al.*, Phys. Rev. Lett. **15**, 429 (1965).
- 1251 [47] D. Casper *et al.*, Phys. Rev. Lett. **66**, 2561 (1991).
- 1252 [48] K. S. Hirata *et al.*, Phys. Lett. B **280**, 146 (1992).
- 1253 [49] Z. Li *et al.*, Physical Review D **98** (2018).
- 1254 [50] Kamiokande Collaboration *et al.*, (2017).
- 1255 [51] T2K Collaboration, Nature **580**, 339 (2020).
- 1256 [52] M. A. Acero *et al.*, Phys. Rev. Lett. **123**, 151803 (2019).
- 1257 [53] M. G. Aartsen *et al.*, Phys. Rev. Lett. **120** (2018).
- 1258 [54] P. Adamson *et al.*, Phys. Rev. Lett. **112** (2014).
- 1259 [55] M. S. Athar *et al.*, Progress in Particle and Nuclear Physics **124**, 103947 (2022).
- 1260 [56] G. Danby *et al.*, Phys. Rev. Lett. **9**, 36 (1962).
- 1261 [57] K. Abe *et al.*, Physical Review D **87** (2013).
- 1262 [58] MINOS Collaboration, D. G. Michael *et al.*, Phys. Rev. Lett. **97**, 191801 (2006).
- 1263 [59] G. Danby *et al.*, Phys. Rev. Lett. **9**, 36 (1962).
- 1264 [60] NOvA Collaboration, M. A. Acero *et al.*, Phys. Rev. Lett. **123**, 151803 (2019).
- 1265 [61] B. Abi, R. Acciarri, M. A. Acero, and G. e. a. Adamov, Eur. Phys. J. C Part. Fields
1266 **80** (2020).
- 1267 [62] Hyper-Kamiokande Proto-Collaboration *et al.*, Prog. Theor. Exp. Phys. **2015**,
1268 53C02 (2015).
- 1269 [63] C. Blanco, D. Hooper, and P. Machado, Physical Review D **101** (2020).
- 1270 [64] MicroBooNE Collaboration *et al.*, Search for an Excess of Electron Neutrino

- Interactions in MicroBooNE Using Multiple Final State Topologies, 2021.
- [65] KARMEN Collaboration, B. Armbruster *et al.*, Phys. Rev. D **65**, 112001 (2002).
- [66] S.-B. Kim, T. Lasserre, and Y. Wang, Adv. High Energy Phys. **2013**, 1 (2013).
- [67] M. Sajjad Athar *et al.*, Prog. Part. Nucl. Phys. **124**, 103947 (2022), 2111.07586.
- [68] K. Abe *et al.*, Nucl. Instrum. Methods Phys. Res. A **1027**, 166248 (2022).
- [69] F. P. An *et al.*, Phys. Rev. Lett. **108**, 171803 (2012).
- [70] RENO Collaboration, J. K. Ahn *et al.*, Phys. Rev. Lett. **108**, 191802 (2012).
- [71] Double Chooz Collaboration, Y. Abe *et al.*, Phys. Rev. Lett. **108**, 131801 (2012).
- [72] J. Collaboration *et al.*, TAO Conceptual Design Report: A Precision Measurement of the Reactor Antineutrino Spectrum with Sub-percent Energy Resolution, 2020, 2005.08745.
- [73] for the RENO Collaboration, New results from RENO and the 5 MeV excess, AIP Publishing LLC, 2015.
- [74] Y. Abe *et al.*, Journal of High Energy Physics **2014** (2014).
- [75] Daya Bay Collaboration, D. Adey *et al.*, Phys. Rev. Lett. **123**, 111801 (2019).
- [76] M. P. Decowski, Nucl. Phys. B. **908**, 52 (2016).
- [77] The KamLAND Collaboration, A. Gando *et al.*, Phys. Rev. D **83**, 052002 (2011).
- [78] Y. Fukuda *et al.*, Phys. Rev. Lett. **81**, 1562 (1998).
- [79] K. Abe *et al.*, Nuclear Instruments and Methods in Physics Research Section A: Accelerators, Spectrometers, Detectors and Associated Equipment **737**, 253 (2014).
- [80] S. Fukuda *et al.*, Nucl. Instrum. Methods Phys. Res. A **501**, 418 (2003).
- [81] Y. Itow *et al.*, (2001).
- [82] M. Jiang *et al.*, Prog. Theor. Exp. Phys. **2019** (2019).
- [83] S. Fukuda *et al.*, Nuclear Instruments and Methods in Physics Research Section A: Accelerators, Spectrometers, Detectors and Associated Equipment **501**, 418 (2003), <http://www.sciencedirect.com/science/article/pii/S016890020300425X>.

- 1298 [84] Y. Nakano *et al.*, Nucl. Instrum. Methods Phys. Res. A **977**, 164297 (2020).
- 1299 [85] Hamamatsu, Hamamatsu Photonics Photomultiplier Tubes Handbook.
- 1300 [86] K. Abe *et al.*, Nucl. Instrum. Methods Phys. Res. A **1027**, 166248 (2022).
- 1301 [87] J. F. Beacom and M. R. Vagins, Phys. Rev. Lett. **93**, 171101 (2004).
- 1302 [88] L. Marti *et al.*, Nucl. Instrum. Methods Phys. Res. A **959**, 163549 (2020).
- 1303 [89] L. Marti *et al.*, (2019).
- 1304 [90] G. Carminati, Phys. Procedia **61**, 666 (2015).
- 1305 [91] T. Tanimori *et al.*, IEEE Transactions on Nuclear Science **36**, 497 (1989).
- 1306 [92] Super-Kamiokande Collaboration, J. Hosaka *et al.*, Phys. Rev. D **73**, 112001
1307 (2006).
- 1308 [93] H. Nishino *et al.*, Nucl. Instrum. Methods Phys. Res. A **610**, 710 (2009).
- 1309 [94] S. Yamada *et al.*, IEEE Transactions on Nuclear Science **57**, 428 (2010).
- 1310 [95] S. Yamada, Y. Hayato, Y. Obayashi, and M. Shiozawa, New online system
1311 without hardware trigger for the Super-Kamiokande experiment, in *2007 IEEE
1312 Nuclear Science Symposium Conference Record*, IEEE, 2007.
- 1313 [96] P. A. Čerenkov, Phys. Rev. **52**, 378 (1937).
- 1314 [97] I. Frank and I. Tamm, Coherent visible radiation of fast electrons passing
1315 through matter, in *Selected Papers*, pp. 29–35, Springer Berlin Heidelberg, Berlin,
1316 Heidelberg, 1991.
- 1317 [98] The T2K Collaboration, KEK Proposal (2001),
1318 <http://neutrino.kek.jp/jhfnu/loi/loi.v2.030528.pdf>.
- 1319 [99] Y. Itow *et al.*, (2001), hep-ex/0106019.
- 1320 [100] The K2K Collaboration and S. H. Ahn, (2001), hep-ex/0103001.
- 1321 [101] The T2K Collaboration, KEK Proposal (2006), http://j-parc.jp/researcher/Hadron/en/pac_0606/pdf/p11-Nishikawa.pdf.
- 1322 [102] T2K Collaboration, K. Abe *et al.*, Phys. Rev. Lett. **112**, 061802 (2014),
1323 <https://link.aps.org/doi/10.1103/PhysRevLett.112.061802>.

- 1325 [103] NINJA Collaboration, T. Fukuda *et al.*, Proposal for precise measurement of
1326 neutrino-water cross-section in NINJA physics run, Proposal for J-PARC and
1327 KEK, 2017.
- 1328 [104] T. Ovsianikova *et al.*, Physics of Particles and Nuclei **48**, 1014 (2017),
1329 <https://doi.org/10.1134/S1063779617060478>.
- 1330 [105] M. Antonova *et al.*, Journal of Instrumentation **12**, C07028 (2017),
1331 <http://stacks.iop.org/1748-0221/12/i=07/a=C07028>.
- 1332 [106] The T2K Collaboration, K. Abe *et al.*, Phys. Rev. D **102**, 012007 (2020).
- 1333 [107] K. Abe *et al.*, Progress of Theoretical and Experimental Physics **2021** (2021).
- 1334 [108] The T2K Collaboration, K. Abe *et al.*, Nuclear Instruments
1335 and Methods in Physics Research Section A: Accelerators, Spec-
1336 trometers, Detectors and Associated Equipment **659**, 106 (2011),
1337 <http://www.sciencedirect.com/science/article/pii/S0168900211011910>.
- 1338 [109] K. Matsuoka *et al.*, Nuclear Instruments and Methods in Physics Research Section
1339 A: Accelerators, Spectrometers, Detectors and Associated Equipment **624**, 591
1340 (2010), <http://www.sciencedirect.com/science/article/pii/S016890021002098X>.
- 1341 [110] K. Abe *et al.*, Phys. Rev. D. **103** (2021).
- 1342 [111] T. Vladislavljevic, *Predicting the T2K neutrino flux and measuring oscillation parame-*
1343 *ters* Springer theses, 1 ed. (Springer Nature, Cham, Switzerland, 2020).
- 1344 [112] D. Beavis, A. Carroll, and I. Chiang, (1995).
- 1345 [113] P.-A. Amaudruz *et al.*, Nuclear Instruments and Methods in Physics Research
1346 Section A: Accelerators, Spectrometers, Detectors and Associated Equipment
1347 **696**, 1 (2012).
- 1348 [114] N. Abgrall *et al.*, Nuclear Instruments and Methods in Physics Research Section
1349 A: Accelerators, Spectrometers, Detectors and Associated Equipment **637**, 25
1350 (2011).
- 1351 [115] S. Assylbekov *et al.*, Nuclear Instruments and Methods in Physics Research
1352 Section A: Accelerators, Spectrometers, Detectors and Associated Equipment
1353 **686**, 48 (2012).
- 1354 [116] D. Allan *et al.*, Journal of Instrumentation **8**, P10019 (2013).

- ₁₃₅₅ [117] F. Vannucci, Advances in High Energy Physics **2014**, 1 (2014).
- ₁₃₅₆ [118] UA1 magnet sets off for a second new life, 2022.
- ₁₃₅₇ [119] S. Aoki *et al.*, Nuclear Instruments and Methods in Physics Research Section
₁₃₅₈ A: Accelerators, Spectrometers, Detectors and Associated Equipment **698**, 135
₁₃₅₉ (2013).
- ₁₃₆₀ [120] M. Yokoyama *et al.*, Nuclear Instruments and Methods in Physics Research
₁₃₆₁ Section A: Accelerators, Spectrometers, Detectors and Associated Equipment
₁₃₆₂ **622**, 567 (2010).
- ₁₃₆₃ [121] K. Suzuki *et al.*, Progress of Theoretical and Experimental Physics **2015**, 53C01
₁₃₆₄ (2015).
- ₁₃₆₅ [122] S. Brooks, A. Gelman, G. L. Jones, and X.-L. Meng, *Handbook of Markov Chain
Monte Carlo* (CRC Press, 2011).
- ₁₃₆₇ [123] W. R. Gilks, S. Richardson, and D. J. Spiegelhalter, *Markov Chain Monte Carlo in
Practice* (Chapman & Hall/CRC Interdisciplinary Statistics, 1995).
- ₁₃₆₉ [124] C. Wret, *Minimising systematic uncertainties in the T2K experiment using near-
detector and external data*, PhD thesis, Imperial College London, 2018.
- ₁₃₇₁ [125] K. E. Duffy, *Measurement of the Neutrino Oscillation Parameters $\sin^2 \theta_{23}$, Δm_{32}^2 ,
 $\sin^2 \theta_{13}$, and δ_{CP} in Neutrino and Antineutrino Oscillation at T2K*, PhD thesis, Oriel
₁₃₇₃ College, University of Oxford, 2016.
- ₁₃₇₄ [126] T. Bayes, Rev. Phil. Trans. Roy. Soc. Lond. **53**, 370 (1764).
- ₁₃₇₅ [127] N. Metropolis, A. W. Rosenbluth, M. N. Rosenbluth, A. H. Teller, and E. Teller,
₁₃₇₆ Journal of Chemical Physics **21** (1970).
- ₁₃₇₇ [128] W. K. Hastings, Biometrika **57** (1970).
- ₁₃₇₈ [129] J. Dunkley, M. Bucher, P. G. Ferreira, K. Moodley, and C. Skordis, Mon. Not. R.
₁₃₇₉ Astron. Soc. **356**, 925 (2005).
- ₁₃₈₀ [130] Particle Data Group *et al.*, Prog. Theor. Exp. Phys. **2020** (2020).
- ₁₃₈₁ [131] H. Jeffreys, *The Theory of Probability* Oxford Classic Texts in the Physical Sciences
₁₃₈₂ (, 1939).
- ₁₃₈₃ [132] R. E. Kass and A. E. Raftery, J. Am. Stat. Assoc. **90**, 773 (1995).

¹³⁸⁴ List of Figures

¹³⁸⁵	1.1	The cross-section of neutrinos from various natural and man-made sources as a function of neutrino energy. Taken from [24]	8
¹³⁸⁶			
¹³⁸⁷	1.2	The solar neutrino flux as a function of neutrino energy for various fusion reactions and decay chains as predicted by the Standard Solar Model. Taken from [25].	9
¹³⁸⁸			
¹³⁸⁹			
¹³⁹⁰	1.3	Left panel: The atmospheric neutrino flux for different neutrino flavours as a function of neutrino energy as predicted by the 2007 Honda model (“This work”) [42], the 2004 Honda model (“HKKM04”) [43], the Bartol model [41] and the FLUKA model [44]. Right panel: The ratio of the muon to electron neutrino flux as predicted by all the quoted models. Both figures taken from [42].	11
¹³⁹¹			
¹³⁹²			
¹³⁹³			
¹³⁹⁴			
¹³⁹⁵			
¹³⁹⁶	1.4	A diagram illustrating the definition of zenith angle as used in the Super Kamiokande experiment [45].	12
¹³⁹⁷			
¹³⁹⁸	1.5	Predictions of the summed neutrino and antineutrino flux for electron and muon neutrinos from the Bartol [41], Honda [42] and FLUKA [44] models as a function of zenith angle with respect to the detector. Left panel: $0.3 < E_\nu < 0.5$. Middle panel: $0.9 < E_\nu < 1.5$. Right panel: $3.0 < E_\nu < 5.0$. Figures taken from [45].	13
¹³⁹⁹			
¹⁴⁰⁰			
¹⁴⁰¹			
¹⁴⁰²			
¹⁴⁰³	1.6	Constraints on the atmospheric oscillation parameters, $\sin^2(\theta_{23})$ and Δm_{23}^2 , from atmospheric and long baseline experiments: SK [50], T2K [51], NO ν A [52], IceCube [53] and MINOS [54]. Figure taken from [55].	14
¹⁴⁰⁴			
¹⁴⁰⁵			
¹⁴⁰⁶	1.7	Reactor electron antineutrino fluxes for ^{235}U (Black), ^{238}U (Green), ^{239}Pu (Purple), and ^{241}Pu (Orange) isotopes. The inverse β -decay cross-section (Blue) and corresponding measurable neutrino spectrum (Red) are also given. Top panel: Schematic of Inverse β -decay interaction including the eventual capture of the emitted neutron. This capture emits a γ -ray which provides a second signal of the event. Taken from [67].	16
¹⁴⁰⁷			
¹⁴⁰⁸			
¹⁴⁰⁹			
¹⁴¹⁰			
¹⁴¹¹			
¹⁴¹²	2.1	A schematic diagram of the Super-Kamiokande Detector. Taken from [81].	19

1413	2.2	The location of “standard PMTs” (red) inside the SK detector. Taken from [79].	21
1414			
1415	2.3	Schematic view of the data flow through the data acquisition and online system. Taken from [94].	24
1416			
1417	2.4	The cross-section view of the Tokai to Kamioka experiment illustrating the beam generation facility at J-PARC, the near detector situated at a baseline of 280m and the Super Kamiokande far detector situated 295km from the beam target.	27
1418			
1419			
1420			
1421	2.5	The near detector suite for the T2K experiment showing the ND280 and INGRID detectors. The distance between the detectors and the beam target is 280m.	28
1422			
1423			
1424	2.6	Top panel: Bird’s eye view of the most relevant part of primary and sec- ondary beamline used within the T2K experiment. The primary beam- line is the main-ring proton synchrotron, kicker magnet, and graphite target. The secondary beamline consists of the three focusing horns, decay volume, and beam dump. Figure taken from [108]. Bottom panel: The side-view of the secondary beamline including the focusing horns, beam dump and neutrino detectors. Figure taken from [109].	29
1425			
1426			
1427			
1428			
1429			
1430			
1431	2.7	The Monte Carlo prediction of the energy spectrum for each flavour of neutrino (ν_e , $\bar{\nu}_e$, ν_μ and $\bar{\nu}_\mu$) in the neutrino dominated beam FHC mode (Left) and antineutrino dominated beam RHC mode (Right) expected at SK. Taken from [110].	31
1432			
1433			
1434			
1435	2.8	Top panel: T2K muon neutrino disappearance probability as a function of neutrino energy. Middle panel: T2K electron neutrino appearance probability as a function of neutrino energy. Bottom panel: The neutrino flux distribution for three different off-axis angles (Arbitrary units) as a function of neutrino energy.	32
1436			
1437			
1438			
1439			
1440	2.9	The components of the ND280 detector. The neutrino beam travels from left to right. Taken from [108].	33
1441			
1442	2.10	Comparison of data to Monte Carlo prediction of integrated deposited energy as a function of track length for particles that stopped in FGD1. Taken from [113].	34
1443			
1444			

1445	2.11 Schematic design of a Time Projection Chamber detector. Taken from [114].	35
1446	2.12 The distribution of energy loss as a function of reconstructed momentum for charged particles passing through the TPC, comparing data to Monte Carlo prediction. Taken from [114].	36
1447		
1448		
1449	2.13 A schematic of the P0D side-view. Taken from [115].	37
1450	2.14 Left panel: The Interactive Neutrino GRID on-axis Detector. 14 modules are arranged in a cross-shape configuration, with the center modules being directly aligned with the on-axis beam. Right panel: The layout of a single module of the INGRID detector. Both figures are recreated from [108].	39
1451		
1452		
1453		
1454		
1455	3.1 Example of using Monte Carlo techniques to find the area under the blue line. The gradient and intercept of the line are 0.4 and 1.0 respectively. The area found to be under the curve using one thousand samples is 29.9 units.	43
1456		
1457		
1458		
1459	3.2 The area under a line of gradient 0.4 and intercept 1.0 for the range $0 \leq x \leq 10$ as calculated using Monte Carlo techniques as a function of the number of samples used in each repetition. The analytical solution to the area is 30 units as given by the red line.	44
1460		
1461		
1462		
1463	3.3 Three MCMC chains, each with a stationary distribution equal to a Gaussian centered at 0 and width 1 (As indicated by the black dotted lines). All of the chains use a Gaussian proposal function but have different widths (or ‘step size σ ’). The top panel has $\sigma = 0.1$, middle panel has $\sigma = 0.5$ and the bottom panel has $\sigma = 5.0$.	48
1464		
1465		
1466		
1467		
1468	3.4 The log-likelihood from the fit detailed in DB: Link to AsimovA Sensitivity Section as a function of the number of steps accumulated in each fit. Many independent MCMC chains were run in parallel and overlaid on this plot. The red line indicates the 1×10^5 step burn-in period after which the log-likelihood becomes stable.	49
1469		
1470		
1471		
1472		

¹⁴⁷⁹ List of Tables

¹⁴⁸⁰ 1.1	Description of the four layers of the Earth invoked within the PREM model [19].	¹⁴⁸¹ 7
¹⁴⁸² 2.1	The various SK periods and respective live-time. The SK-VI live-time is calculated until 1 st April 2022. SK-VII started during the writing of this thesis.	¹⁴⁸³ 18
¹⁴⁸⁵ 2.2	The trigger thresholds and extended time windows saved around an event which were utilised throughout the SK-IV period. The exact thresholds can change and the values listed here represent the thresholds at the start and end of the SK-IV period.	¹⁴⁸⁶ 25
¹⁴⁸⁹ 2.3	The threshold momentum and energy for a particle to generate Cherenkov light in ultrapure water, as calculated in Equation 2.2 in ultrapure water which has refractive index $n = 1.33$	¹⁴⁹⁰ 26
¹⁴⁹² 3.1	Jeffreys scale for strength of preference for two models A and B as a function of the calculated Bayes factor ($B_{AB} = B(A/B)$) between the two models [131]. The original scale is given in terms of $\log_{10}(B(A/B))$ but converted to linear scale for easy comparison throughout this thesis.	¹⁴⁹³ 53
¹⁴⁹⁴		¹⁴⁹⁵